The role of solar wind in the formation of hydroxyl on airless silicate bodies in space

A Thesis

Presented to

the faculty of the School of Engineering and Applied Science

University of Virginia

in partial fulfillment

of the requirements for the degree

Master of Science

by

Micah J. Schaible

May

2014

APPROVAL SHEET

The thesis

is submitted in partial fulfillment of the requirements

for the degree of

Master of Science

Micah J. Schaible

AUTHOR

The thesis has been read and approved by the examining committee:

Raúl A. Baragiola

Advisor

Robert Johnson

Jongsoo Yoon

Accepted for the School of Engineering and Applied Science:

James H. Ayl

Dean, School of Engineering and Applied Science

May

2014

Dedicated to all individuals who work for the betterment of themselves, their world, and their connection with the oneness that binds us all. To all my family and friends that have seen my needs and helped me to the position I am in, thank you.

Abstract

Studies of the interaction of solar radiation with the surfaces of moons, asteroids and comets can provide fundamental information about the early history of our solar system and help elucidate the ways in which such systems evolve. Airless bodies in space such as the Moon, asteroids and interplanetary dust particles are subject to bombardment from energetic solar wind electrons and ions, ultraviolet photons, micrometeorites and cosmic rays. This process is known as *space weathering* and the cumulative effect of the radiation modifies the chemical and physical nature of the ices and minerals that make up such surfaces. The work presented here investigates the interaction of solar wind hydrogen and helium with analog minerals and lunar soil using infrared spectroscopy (FTIR), mass spectrometry (SIMS), and optical photometry. Experiments were performed under Ultra High Vacuum (UHV) pressures and over a temperature range of 15 K to 400 K to simulate lunar surface conditions, and radiation was performed using a mass analyzed ion accelerator that allowed samples to be irradiated with specific ions at energies in the range of the solar wind.

Radiation of surfaces in vacuum causes both formation and removal of atomic and molecular species. The sputtering rate of water from regolith surfaces was measured by first dosing un-compacted lunar soil with water and subsequently irradiating with 4 keV He^+ ions to determine a sputtering cross section for molecules on the surface of grains. The amount of water present on the grains was determined by using X-ray Photoelectron Spectroscopy (XPS) to monitor the atomic percentage of oxygen on the surface in relation to silicon, and the composition of sputtered species and the ejection energy of surface ions were measured using SIMS and provide an estimate of the solar wind sputtering contribution to the lunar exosphere. Using the measured cross-section, the lifetime of a water molecule of the surface of a grain is 29 years at the lunar equator and decreases to an estimated ~12 years based on the additional contribution of hydrogen ion sputtering.

To simulate solar wind implantation on the lunar surface and investigate the effects of ion radiation on hydroxyl (deuteroxyl) concentration, thin sections of minerals and lunar rocks (100-200 μm thickness) were irradiated with 2-5 keV H^+, D^+ and He^+ ions. Implanted H (D) ions were found to chemically bond with oxygen in the silicate samples, causing changes in the absorption spectra of the samples at 2.7 μm (3.1 μm) attributed to the OH (OD) stretch vibration, while He^+ irradiation caused no changes in this band. The initial yield (OH formed per incident ion) was ~90% and the OH (OD) absorption band was found to saturate at implantation fluences of ~$2x10^{17}$ H(D)/cm^2. Irradiation also modified the Si-O stretch band at 9.2 μm causing the peak height to decrease and the FWHM to increase, and both yield and Si-O peak height decreased exponentially with increasing fluence. These measurements allow constraints to be placed on solar wind contribution to observational and theoretical models of water on the lunar surface.

Contents

1   Introduction

Understanding the interaction of solar radiation with the surfaces of moons, asteroids and comets can provide fundamental information about the early history of our solar system and help elucidate the ways in which these systems evolve. In addition to electromagnetic radiation (photons), the sun emits energy in the form of energetic ions and electrons called the *solar wind* which stream out from the solar corona and impact the materials that they come into contact with in interplanetary space. The ions of the solar wind consist mainly of hydrogen (protons, ~92%) and helium (~8%), with other trace components of carbon, neon and argon. In addition to the solar wind, micrometeorites can impact the surfaces of atmosphereless solar system bodies causing structural changes in the material. *Space weathering* is the term used to describe the cumulative effect of energetic solar wind electrons and ions, ultraviolet photons, micrometeorites and cosmic rays constantly impacting the surfaces of airless bodies in the space environment. This complex interplay of implanted ions, heating from micrometeorite impacts and photoionization by UV radiation causes chemical and physical changes in the constituent minerals or ices [Hapke, 2001; Bennet et al, 2013] as identified in space by the optical properties of the surface [i.e. Peiters et al, 1993] and drives the evolution from basic elemental materials toward more complex molecular formations [Greenberg and Li, 1999]. On the Moon and some asteroids, comminution, agglutination and solar wind spallation process the surface materials, breaking and intermixing rocks and minerals creating a fine grained a layer of loose material called the *regolith*, and ejection of surface species due to energetic irradiation causes a tenuous atmosphere, called an *exosphere*, to form.

A detailed understanding of energetic stellar particle interactions with solid materials in space is needed to accurately model the chemical and geologic evolution of planetary systems. When the size of the irradiated bodies is either very large (>1e6 m) or very small (<1e-6 m), as in a planet or interstellar dust respectively, the radiation interactions are predominantly with other atoms and molecules in the gas phase (i.e. the planetary atmosphere or interstellar gas). For intermediate sized objects that lack a gaseous atmosphere, charged particles embed themselves into the regolith. The implanted ions cause changes to the target atoms through electronic excitations and nuclear displacements, and can combine with defects of the damaged mineral lattice to form new molecules that are otherwise absent from the host material [Bennet et al, 2006; Baragiola et al, 2005, Strazzula et al, 1995]. In addition to understanding the result of material processing from radiation damage and collisions with other solid objects, it is important to understand how these environments behave for the purpose of robotic or human exploration and to minimize potential hazards such as lunar dust clinging to the surfaces of exploration vehicles. Studying the mechanisms of space weathering under laboratory conditions similar to those encountered in space helps create a clear understanding of these complicated processes and can place constraints on relative contributions used in computational models.

The work presented here simulates the interaction of solar wind ions with analog minerals, similar in composition to materials in space but of terrestrial origin, and actual lunar soil returned during the NASA Apollo missions. Analyses using infrared spectroscopy, mass spectrometry, and optical photometry were carried out to determine how the radiation processes effect hydroxyl and water in the samples. Experiments were performed under Ultra High Vacuum (UHV) pressures (<1x10^{-9} Torr) to avoid

atmospheric contamination, and the effect of temperature was investigated by cooling and heating the sample to <50 K and >400 K, equivalent to lunar surface extremes, using a cryogenic refrigerator and resistive heaters respectively. In addition to an exposition of the investigations performed, this document will serve as a review of the design and function of an experimental system constructed to be able to carry out a wide variety of physical simulations relevant to astrochemistry and space weathering. A major effort not immediately apparent in the document has been refitting a lab space to house the system, from hanging water cooling hoses and wiring electrical connections to installing an overhead crane to lift the cryogenic cold head from the main chamber. Many of the main system components were designed and constructed by the author or built by the in-house machinists at UVa, although the major experimental apparatuses such as the UHV chamber and infrared spectrometer were purchased from vendors, and the names of manufacturers and vendors is given. The system was literally built from the ground up, with nearly the entirety of the work being carried out by solely the author. A description of the design, the main experimentally motivated features and the commissioning of each system will be given along with detailed drawings of custom designed parts.

2   Astrophysical Motivation

Interstellar dust and the surfaces of atmosphereless bodies in space experience extreme conditions of pressure and temperature and are subject to a wide variety of energetic irradiation sources [Leroux, 2009]. In dark protoplanetary clouds and in permanently shadowed regions of moons or asteroids, temperatures are cold enough to freeze out most volatile species and icy mantles accumulate on top of silicate or carbonaceous grains. At the same time, due to the lack of a significant atmosphere, the ions and electrons of the solar wind impact the surface and enter the solid, subsequently losing energy through elastic (knock-on) and inelastic (electronic excitation) collisions leading to ionization, excitation, and nuclear displacement of the target material. Energy deposited by these processes causes radiation damage and amorphization of crystalline materials, and once the implanted particle has lost sufficient energy to the medium it may participate in chemical reactions. In addition, both solar and extrasolar photons can modify the uppermost surface; photons with energies <30-100 keV are directly absorbed on interaction with the material and cause either transitional excitations (electronic, vibrational and rotational) or emission of electrons (photoionization) in the constituent atoms, while higher energy photons experience energy loss through scattering processes before being absorbed. The goal of experimental astrophysics is to create analogs of space environments in the laboratory in an attempt model these processes and better understand their physical characteristics and evolution by measuring fundamental rate constants, formation products, and physical properties in a way that can contribute to the explanation of telescope and satellite observations and measurements, as well as constrain computational models of the chemical and physical evolution of the planetary environment.

The lunar surface provides an ideal system for study of space weathering effects given its proximity to Earth and our ability to obtain a detailed knowledge of its composition and evolution through study of returned soil samples. All of the above mentioned space weathering processes are present on the surface of the Moon, and numerous spacecraft and telescope measurements carried out

for over half a century have provided detailed information on the variation in surface and exosphere composition. For several decades following the Apollo missions to the Moon, the lunar surface was considered to be anhydrous and largely devoid of volatile species. Though it was thought since the 1960s that cold traps at the lunar poles could potentially hold large deposits of water [Watson, 1961; Arnold, 1979], analysis of returned lunar samples from the Apollo era led to a general consensus that the bulk of the moon was nearly completely anhydrous [G. Heiken et al, 1991; Epstein and Taylor, 1974, 1975; Taylor et al, 1995]. In the last five years this view has changed, and a new paradigm containing three distinct collections of lunar water - bulk, surficial, and polar - has emerged. Measurements of volatile species in returned lunar soils and mineral grains found H concentrations that correspond to ~10 ppmw H_2O in lunar volcanic glasses to >1000 ppmw H_2O in lunar apatites [$Ca_5(PO_4)_3(F,Cl,OH)$], comparable to volcanic rocks on Earth [Saal et al, 2008; Liu et al, 2012; Boyce et al, 2010]. These results led to predictions that the bulk Moon could hold water concentrations comparable to rocks in the Earth's crust. Additionally, the existence of polar water was confirmed when the LCROSS spacecraft was crashed into the permanently shadowed crater Cabeus on the lunar south pole resulting in a vapor plume which showed water present at an estimated 5-6% by mass [Colaprete et al, 2010; Strycker et al, 2013].

The third source, surficial water, was identified in 2009 when data from instruments onboard the Chandraayan-1 (M^3), Deep Impact (EPOXI), and Cassini (VIMS) spacecraft revealed a 3 μm absorption signal present across the lunar surface (Figure 1) [Pieters et al, 2009; Sunshine et al, 2009; Clark, 2009]. The absorption depth increased toward higher latitudes and was attributed to OH or molecular water on the surface of soil grains in the top ~3 mm of the lunar regolith [Pieters et al, 2009]. Comet and asteroid impactors and interior degassing were unable to explain the variations in signal strength with composition [McCord et al, 2011] and time of day [Sunshine et al, 2009], and the combination of solar wind hydrogen with oxygen from the lunar soil was hypothesized to explain the signal. The hypothesis of OH formation on the Moon due to solar hydrogen implantation was proposed in each of the three 2009 papers, then discussed in greater detail with regard to the M^3 data by McCord et al (2011) who distinguished distinct absorptions at 3um and 2.8um. The 3um absorption was present only at higher latitudes while the 2.8um absorption, although less intense, was present even at the equator. Complicating the interpretation of the signal were the effects of surface geometry and thermal emission corrections [Besse et al, 2013; Clark et al, 2011].
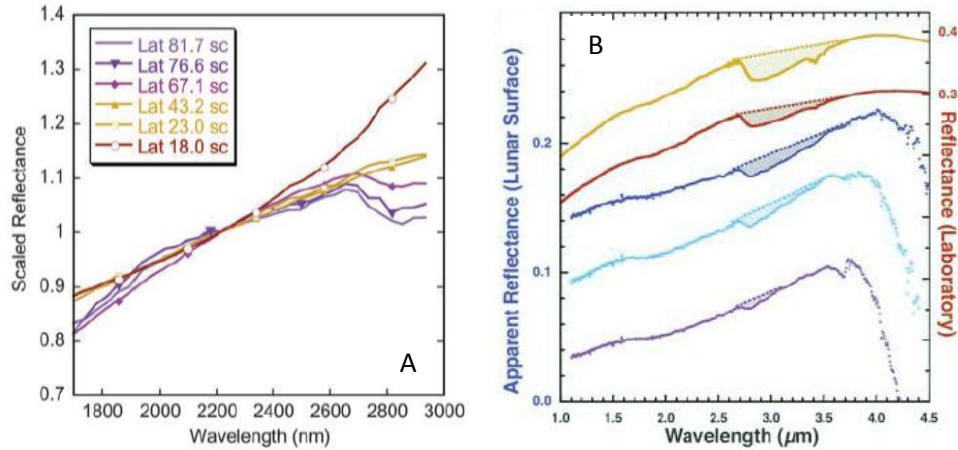
Figure 1: Lunar surface spectra from instruments aboard two different spacecraft. (A) Data from the M^3 instrument on Chandryaan-1 with the latitude at which each spectra was taken indicated in the legend [Pieters et al, 2009]. (B) Spectra taken by the EPOXI camera on Deep Impact during three lunar passes and for two laboratory spectra (14259, red; 62231, orange) [Sunshine et al, 2009]. These spectra show absorption bands at 2.8-3 µm that were attibuted to the OH stretch absorption due to hydroxyl or water being present in the lunar regolith.

The solar wind ions arrive at the lunar surface with an average flux of 1×10^8 ions cm^{-2} s^{-1} and an average energy of 1 keV/amu. The impinging ions are neutralized as they approach the surface, and subsequently lose energy through collisions with electrons and atoms, eventually coming to a rest at a depth dependent on ion energy and type of material [Johnson, 1990]. At the end of their trajectory, the implanted ions can chemically combine with lattice atoms to form new molecular species [i.e. Bibring et al, 1982] or become trapped in radiation defects and interstitial sites. Hydrogen makes up over 90% of the solar wind composition and bonds with many atoms that make up the bulk of solid objects in space (i.e. carbon, nitrogen and silicon) and thus understanding what bonds can form and determining reaction cross-sections is necessary to explain the molecular content of silicates of the lunar regolith. For example, MeV hydrogen implanted into lunar simulant glasses can become trapped by bonding to oxygen atoms to form OH, creating a distribution of hydroxyl molecules throughout the implanted region [Zeller et al, 1966]. While in principle it is possible for hydrogen to bond directly to silicon as well [Moore et al, 1991], the formation of SiH in silicates due to ion implantation has not been detected [Buemi et al., 1993; Djouadi et al, 2011]. Thus, trapping of implanted hydrogen as a result of radiation induced chemical bonding can be thought of as limited by the volume concentration of oxygen, N_o, in the silicate sample [$N_o \sim 2 \times 10^{22}$ (4×10^{22}) SiO$_2$ (-O)/cm^3]. At implantation energies of 150-300 keV, the formation rate of bound hydrogen decreases after implantation fluences $\geq 2 \times 10^{17}$ H$^+$/cm^2 indicates a saturation in the formation of OH bonds, and with further irradiation the hydrogen either accumulates in radiation induced 'bubbles' or diffuses through the material and escapes, likely as H$_2$ or H$_2$O [Mattern et al, 1976]. Though it has long been established that that higher energy hydrogen implantation can produce hydroxyl in silicates, studies are needed at solar wind energies.

Radiation produces amorphization of the target material through atomic displacements, and amorphous rims (radiation induced) of h ~ 100 nm thickness have been measured in lunar grains and provide a convenient depth for consideration of hydrogen behavior in implanted minerals [Keller and

McKay, 1997]. Noticeable diffusion of implanted species occurs for both 30 keV H implanted in OH saturated amorphous SiO_2 (penetration depth of h ~ 400 nm) [Fink et al, 1995] and for 20-200 keV He implanted in olivine (penetration depth h ~ 100-200 nm) [Futagami et al, 1993]. The diffusion coefficient D_H for H in SiO_2 was found to be ~10^{-14} cm^2/s at temperatures of 400 K [Fink et al, 1995] while for H_2 in vitreous silica it is found by extrapolation to be D_{H2} ~10^{-9} cm^2/s [Shang et al, 2009]. For anhydrous silicates with low hydroxyl concentration, chemical and radiation induced trapping of the implanted H could significantly reduce the diffusion coefficient meaning that, up to the saturation fluence, trapped OH in pristine minerals should be stable through a lunar day. Above the saturation fluence, additional hydrogen diffuses through the soil with a characteristic time of escape τ_{escape} ~ h^2/D_{H2} < 1s, where h is the original depth of the H, and leaves the material as H_2 or H_2O [Morimoto et al, 1992] from samples that have not been radiation damaged. Assuming that up to half of the oxygen in the silicate material can bind to implanted hydrogen, as suggested by high energy saturation measurements [Mattern et al, 1976] and that the implanted region has a uniform concentration of hydrogen up to a depth of h = 100 nm, the saturation column density is estimated to be η = 0.5*N_O*h = $1x10^{17}$ OH/cm^2. Heating from micrometeorite impacts can vaporize the surrounding area, liberating volatiles from the bulk and redepositing the material on surrounding grains as amorphous (vapor deposited) rims [Keller and McKay, 1997]. In addition to covering previously implanted regions of the grains, the amorphous rims could themselves contain OH transported with the vaporized materials [Crider and Vondrak, 2000] or formed from solar wind implantation, thus potentially creating regions hundreds of nm thick of OH and H_2O containing material. As a result of meteorite gardening burying implanted grains and exposing fresh soil, the predicted solar wind hydrogen implantation could produce as much as 1% of water in the upper ~40 cm of the lunar regolith [Starukhina, 2001], consistent with epithermal neutron measurements from the Lunar Prospector of hydrogen concentration in the lunar regolith [Feldman et al, 2000].

In addition to formation at the surface, water has been delivered to the lunar surface in its geologic history by comets and meteorites, and micrometeorites still constitute a significant source of delivery [Ong et al, 2010]. Water carried to the lunar surface in comets and meteorites is released on impact and can diffuse over wide areas, eventually coming to rest on the surface of regolith grains. Furthermore, several recent publications show that water contents in returned lunar glasses and mineral grain inclusions could reach levels similar to that in terrestrial rocks (10-1000 ppmw) [Saal et al, 2008; Liu et al, 2012], and this bulk water could diffuse through the lunar soil until it reaches the surface where it is exposed to incoming radiation. Even if the surface species are shielded from solar radiation, cosmic rays and the background UV field ensure at least a slow rate of modification through knock-on collisions, electronic excitations, secondary collisions with emitted electrons, and the destruction/redistribution of molecular bonds, as well as removal and possible re-deposition on adjacent grains and exposure of fresh surfaces due to micrometeorite impact gardening. These processes can transfer energy to a surface molecule and, if the molecule is located in the upper few monolayers of the grains, it can be ejected with a velocity dependent on the excitation energy and adhesion strength to the surface [Andersson and van Dishoeck, 2008]. For example, when an atom near the surface absorbs a photon an electron may be emitted, and this electron can subsequently excite and remove atoms and molecules either as neutral or ionized species. Likewise, solar wind ions can remove molecules from the surface of grains by sputtering [Shi et al, 1995]. If the molecule is ejected with

insufficient energy to escape the gravity well of the body, it will travel ballistically in a random hop process across the surface until it is either lost to space or trapped at the poles. Thus, both photodesorption and ion sputtering could act as a driver for migration of water molecules to the polar cold traps.

Models of volatile migration on airless bodies require knowledge of desorption cross sections, and while many measurements of sputtering yield have been made from optically flat surfaces [i.e. Famá et al, 2008], the lunar regolith is predominantly a fine powder with a median particle size of 40 to 130 µm [Lunar sourcebook]. Shadowing effects due to irregular surfaces and multiple grains have an estimated effect of decreasing desorption yield by a factor of ~3 [Cassidy and Johnson, 2005]. Though experimental measurements of sputter redeposition in compressed powders yields values similar to the predicted [Loeffler et al, 2009], sputtering cross-sections from loose granular surfaces is sparse. Photodesorption by solar UV photons was found to be the process that ultimately limits the lifetime of a water molecule on the surface of a grain at the lunar equator, and the lifetime of an exposed water molecule was found to be only 14 hrs [Mitchell et al, 2013], though sputter removal could also be an important mechanism in shadowed polar craters where electric fields generated by solar wind plasma expansion may cause ions to be accelerated into the crater [Zimmerman et al, 2011]. Therefore, the current work measured the sputtering cross-section of water under 1 keV hydrogen bombardment from the surface of loose lunar soil and in addition to hydroxyl formation rates in the bulk of Si-O containing thin sections.

Constraining the water concentration on the lunar surface can be done by measuring the water content of returned lunar soils or to carry out irradiations experiments on analog minerals in the laboratory. Liu et al (2012) measured an absorption band at 2.8 µm in glassy inclusions of mature lunar grains and found absorption on the order of 0.01 absorbance units (a.u) corresponding to 2% transmittance or ~1×10^{17} OH/cm^2, somewhat lower than lunar surface measurements. Recent laboratory experiments that have tried to produce OH/H$_2$O bands by H$^+$ implantation in silicates have found contradictory results, and the divergence was attributed to differences in the implanted materials and differing experimental conditions. Reports by Managadze et al (2010) and Ichimura et al. (2012) show OH/OD formation after irradiating lunar soil simulants with keV energy hydrogen (deuterium) ions. Managadze et al used Secondary Ion Mass Spectrometry (SIMS) to detect sputtered water ions from lunar simulants but did not correlate them to IR measurements. SIMS is orders of magnitude more sensitive than IR absorption and thus a small SIMS signal may not give an observable signal in IR. Ichimura et al (2012) irradiated fine grained (<45 µm) lunar soil to fluences of ~10^{17} H$^+$/cm^2 and, using ex situ diffuse IR reflectance, measured hydroxyl band depth increases of 4-5% relative to a dehydroxylated sample. However, because the irradiations were not done under ultra-high vacuum conditions and samples were exposed to air several times during the experiment, and additionally because of possible contamination of the ion beam with OH$^+$ (OD$^+$) ions in both studies, the assertion that ion irradiation under lunar conditions can produce sufficient OH to account for the remote IR observations of the Moon remained questionable. Meanwhile, Burke et al (2011), using thin slabs of terrestrial ilmenite and anorthite under UHV, obtained an upper limit on OH production that predicted

lunar absorption band depths in the Moon of no more than 0.5% reflectance or ~2×10^{16} OH/cm^2, much lower than the remote lunar measurements of 3-14% reflectance.

In addition to changes in the 3 µm OH band, the Si-O stretch band at ~10 µm also changes as a result of ion irradiation. Minerals irradiated with keV energy H^+ and He^+ ions amorphize at fluences < 1×10^{18} ion/cm^2 [Demyk et al, 2004] as evidenced by the smoothing of Si-O bands from 9-13 µm. An increased OH concentration of plasma deposited SiO_2 causes a shift in the Si-O peak towards lower wavenumbers and a narrowing of the band [Gupta and Parsons, 2000]. The hydroxyl peak at 2.7 µm was found to shift peak position depending on whether the hydroxyl molecules were present in large enough concentrations for significant interactions between molecules to be present. The OH peak at ~$3650 cm^{-1}$ is typically assigned to 'un-associated' Si-OH bonds, meaning that no significant hydrogen bonding is present, while the symmetric stretch at ~3450 cm^{-1} is assigned to associated SiOH bonds [Gupta and Parsons, 2000].

Complicating laboratory measurements on returned lunar samples and air exposed samples is the fact that irradiated surfaces are more prone to atmospheric contamination due to increased diffusion and penetration of atmospheric species, as well as enhanced surface reactivity. Irradiation causes chemical changes in the irradiated region of silicates [Dukes et al, 1999; Daviosne et al, 2008] as well as enhances the reactivity of the surface [Lanford and Burman, 1983; Cantando et al, 2008] including the potential to form OH bonds [Gruen et al, 1976] and increases diffusivity [Dienes and Damask, 1958]. Samples returned during the Apollo era have been in storage for over 40 years, and even though they have been stored in a nitrogen purged atmosphere, trace amounts of water vapor and hydrogen could diffuse into the materials. Materials collected from the lunar surface have had their atomic bonding arrangement altered by energetic radiation which could leave a material in a stable but high energy state, thus increasing the probability of reaction with an additional implanted atoms or diffusion species.

The goal of the current work was not to reproduce the environment analyzed by the spacecraft observations but to carry out well controlled experiments to understand and quantify the radiation chemistry of silicates implanted with keV ions. The focus of the investigation was hydroxyl production in silicates and the physical process of OH formation and trapping in minerals, with complementary measurements of water sputtering from lunar soils to understand removal by ion bombardment. In earlier experiments, spectroscopy measurements were taken in reflectance where the optical path length is not well determined, while the current analyses were done using transmission geometry for which there is a well-defined optical path. Using materials of known composition and monitoring changes during irradiation allow precise production rates and upper limits on hydroxyl concentration in lunar soils to be determined. These results are applicable to the Moon and also to other airless bodies such as Mercury, main belt asteroids [Starukhina, 2001], and in protoplanetary silicate grains [Djouadi et al, 2011] subject to stellar proton irradiation. Though measurements on SiO_2 and olivine allow for estimates of hydroxyl production on silicate bodies, they are only a small sampling of the variety of extant minerals in space and composed of only a single mineral type whereas extraterrestrial materials (e.g. lunar breccias) are agglomerations of multiple minerals held together by a glassy matrix. Thus, further studies on additional astrophysically relevant minerals and glasses under UHV conditions are

needed to constrain formation rates of OH and to determine if solar wind implantation can account for the reported lunar signals.

3   Experimental Design

Despite careful preparation and state-of-the-art techniques, astrophysical processes cannot be perfectly simulated in the laboratory due to the extremes in pressure, the complex interplay of various energy sources, and the timescales involved. Spurious measurements may result from reactions between the system of interest and terrestrial contaminates such as atmospheric water vapor and hydrocarbons [i.e. Lanford and Burman, 1983; Cantando et al, 2008; Gruen et al, 1976], and reproducing irradiation sources capable of simultaneously supplying multiple ion types as well as photons and electrons is beyond present capabilities. Despite these difficulties, experimental innovations of the last several decades have resulted in a number of fundamental measurements of reaction rates [Martinez et al, 2009; Ioppolo et al, 2008], product yields for various types of radiation [Loeffler et al, 2006; Oberg et al, 2009a], desorption yields [Oberg et al, 2009b; Dukes et al, 2011] and charging properties [Shi et al, 2012]. The design of experimental systems typically involves UHV chambers capable of maintaining minimum pressures on the order of $1x10^{-10}$ Torr (~$3.3x10^6$ particles/cm^3). The chambers are pumped via momentum transfer (turbo molecular pumps), ionization of residual gas molecules and implantation in solid electrodes to remove them from vacuum (ion pumps), usually combined with a method of gettering to trap reactive light reactive gases (He and H_2), or using cryopumps in which a metallic array is cooled to <15 K and freezes out residual gases. In addition, closed circulation helium systems allow cryogenic temperatures (<10 K) to be routinely achieved for ice and mineral samples. Ices can be prepared in situ by leaking high purity gases onto a cooled metallic, carbonaceous or mineral substrate through directed molecular dosing or from atom sources, while mineral systems are prepared externally as thin sections by cutting or grinding samples or by sprinkling powders onto adhesives or pressing them into molds. Externally prepared samples are often cleaned by vacuum baking or ion sputtering to remove surface contaminates prior to processing and analysis. Lyman-α UV lamps, ion accelerators and electron guns meant to simulate solar and other energetic sources (i.e. planetary magnetospheres) are used to irradiate the samples while spectroscopy, microgravimetry, and gas phase detection of sputtered surface species are used to monitor changes in the physical and chemical state.

Analysis systems have become increasingly sophisticated and can achieve typical sensitivities at the molecular level [see, for example, Allodi et al, 2013]. One technique used both in the laboratory and for the observation of astronomical objects is spectroscopy wherein the constituents of the system are analyzed by collecting either the reflected or transmitted components of a broad spectrum light source from a specific region of interest then and directing the light to a photosensitive detector. The molecules in the material absorb light through vibrational excitations of the molecular bonds, and constituents are identified by absorption patterns appearing at specific wavelengths of light. Fourier Transform Infra Red (FTIR) spectroscopy is a commonly used laboratory technique that allows changes due to radiation to be determined by a change in the spectra of light either reflected, transmitted, or thermally emitted by the sample. Similarly, X-ray Photoelectron Spectroscopy (XPS) directs a beam of monoenergetic x-rays onto a sample which causes core electrons to be ejected from atoms. Electrons

emitted from near-surface atoms (top ~10-15 monolayers) can escape the solid without energy loss, and these electrons are passed through a spherical or cylindrical energy analyzer and collected by an electron multiplier. Peaks at specific energies in the resulting signal are diagnostic of the surface atomic composition and the chemical state (bonding) of the species. Another technique used to analyze the uppermost surface is Secondary Ion Mass Spectrometry (SIMS). In SIMS, a source accelerates ions, often Argon or Cesium, toward the target where they impact the surface and lose energy either through momentum transfer or electronic excitations. Some of the energy transferred to the surface can result in molecules and atoms being emitted as either neutral or ionized species. SIMS detects the ejected ions and can be used to create a detailed profile of the composition of the target as a function of depth.

These diverse experimental techniques are often combined in a single vacuum system capable of carrying out complementary measurements on a sample processed by heating and cooling, irradiation and exposure to molecular gas such that these processing and analysis can be performed in any order without ever exposing the sample system to terrestrial contaminates. Such a system was constructed in the Laboratory for Atomic and Surface Physics (LASP) at the University of Virginia, Thornton Hall, B-wing. The system consists of a stainless steel UHV chamber capable of maintaining pressures $<5x10^{-10}$ Torr and is equipped with a unique sample transfer system that can rapidly exchange samples into and out of vacuum on molybdenum transfer flags without raising the main chamber pressure above $1x10^{-6}$ Torr, thereby minimizing surface contaminates due to atmospheric exposure. By not exposing the chamber to atmosphere, a return to base pressures can be achieved in < 1 hour. A closed-cycle helium cryostat was installed and is able to cool the sample holder, and temperatures of <10 K can be maintained throughout the duration of the experiment. In order to simulate the solar wind, an ion accelerator containing a duo-plasmatron ion source and a velocity filter for ion selection was assembled and attached to the UHV chamber. The accelerator can provide a current of tens of nano amps at the sample for energies <5 keV, with larger currents achievable at higher energies. The primary analysis equipment attached to the system consists of the following: an Thermo-Nicolet FTIR spectrometer that can be used in either transmission or reflection mode for detecting chemical changes in the samples, as evidenced by changes in IR absorption bands; an Extrel Analytical SIMS for detecting desorbed molecular species and ejected secondary ions during irradiation; and an Inficon Quartz Crystal Microbalance (QCM) embedded in the main sample holder for accurately measuring the mass or thickness of deposited gaseous species. The sample holder can be configured so that either two spring clips or a 90% transmittance Ni wire grid can be used for securely pressing the transfer flag against the cooled sample holder, and in the middle of the flag is 10 mm hole through which the IR light can pass during transmission experiments several silicon diodes for temperature monitoring, heaters for warming the sample to a controlled temperature, and a Faraday cup for current measurement (Figure 2). A dual-tip molecular gas doser was designed and constructed to deposit ices simultaneously on the QCM and transfer flag, allowing precise control over the thickness of deposited material on mineral and glasses. Each of these systems is described in detail below and the salient design features presented. The author was the lead designer and performed most of the construction on the system including refitting of the lab space to provide cooling and electrical requirements, mounting and supporting major analysis equipment, and machining of some components, although the work benefitted greatly from collaborations with Peter Schare, Cathy Dukes, Ujwal Raut and others at the LASP.

Instrument controller stacks, pump controllers, and pico-ammeter for ion beam current measurement

Janis Research Company Cryogenic Cold Head

Electrical Connections from external controllers to sample holder

XYZ Manipulator and 360° differentially pumped rotation stage

FTIR exit optics and detector

Peabody 1-25 keV Ion Accelerator

Thermo-Nicolet FTIR Spectrometer (not visible) and entrance optics

Custom Molecular Gas Doser

Pressure measurement instruments including quadrupole gas analyzer

Magnetically coupled sample transfer arm and differentially pumped introduction stage

Cryogenic pump (under bench), turbo molecular pump, and roughing pump (not shown)

Silicon diodes for temperature measurement (embedded)

Connection to second stage cold finger
- Sapphire washers used for electrical isolation

Quartz crystal microbalance

Leads for sample heater (on reverse of sample holder)

Removable sample flag w/ olivine sample over transmission hole

~3mm dia. FTIR beam spot

Faraday cup w/ 1mm aperture for ion beam current/flux measurement

Figure 2: (Top) Experimental system with major components labeled. (Bottom) Custom designed sample holder capable of spectroscopy, thermal desorption, and ion beam current measurements for ice and mineral sample analyses.

3.1   System Design Components

3.1.1   Pumping and pressure measurement

The UHV chamber (MDC) was a 12 in. stainless steel sphere onto which were welded a number of metal sealed conflat vacuum ports (Figure 3). Pressures as low as 1×10^{-6} Torr could be reached using a 30 L/s turbo molecular pump (TPU 55, Pfeiffer-Balzers) connected to the lower hemisphere of the chamber through a 2.75 in. port and backed by oil free scroll pump (Edwards). A 4000 L/s (water) cryogenic pump (Cryotorr 8, CTI-Cryogenics) was mounted onto the bottommost 10 in. port and could be separated from the main chamber by means of a large gate valve. The main chamber was first pumped to high vacuum pressures ($<1\times10^{-6}$ Torr) using only the turbo and roughing pumps, then the cryopump was switched on and the turbo pump sealed off from the system. In order to reach base pressures $<10^{-9}$ Torr, the system was baked at ~150 C for >48 hours by wrapping resistive heating tapes around the chamber, ports, and attached instruments exposed to vacuum, then covering these in aluminum foil to distribute heat evenly across the surface. Pressure was measured independently in both the pre-chamber and the main chamber using a nude ion gauge connected to an external gauge controller (DGCIII, Perkin-Elmer), and relative partial pressures of the residual gases were monitored using a small quadrupole mass spectrometer (QMS) equipped with an ionization source and a Faraday cup for current measurements (Dycor LC series, Ametek). The same roughing and turbo pump were also used to pump the gas manifold, from which high purity gases could be leaked to specific pressures into the chamber, and the differentially pumped seal on the 360° rotation stage (Figure 4).
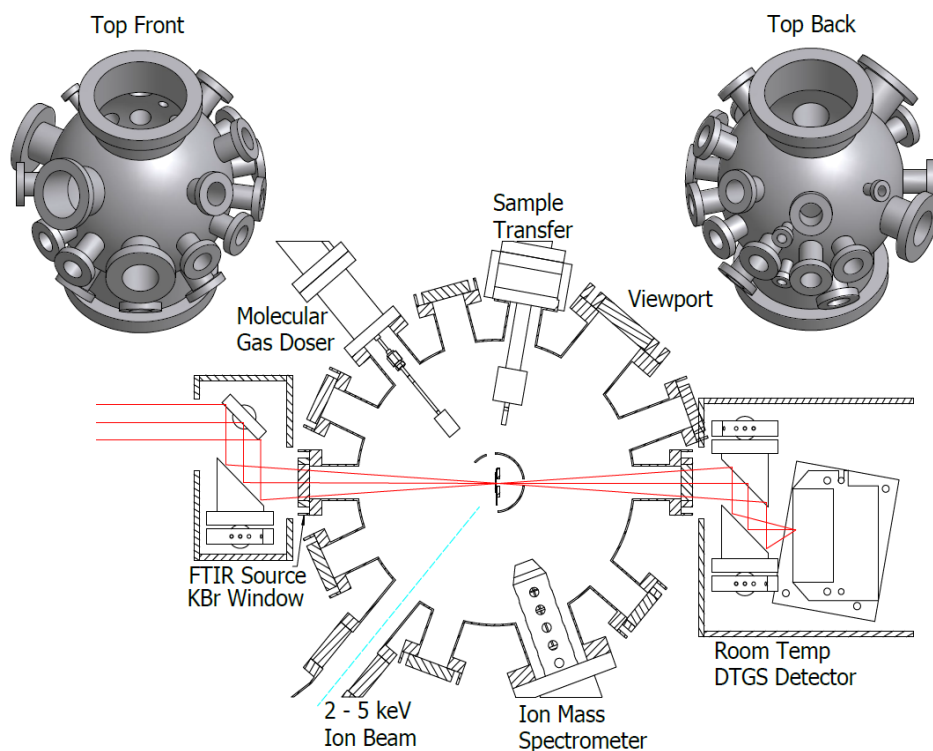

Figure 3: Three dimension CAD models of the chamber showing the arrangement of ports for analysis equipment, pumping, sample manipulation and viewing. Also shown is a cross-section of the equator of the sphere where the irradiation, deposition, and analysis equipment are aligned.
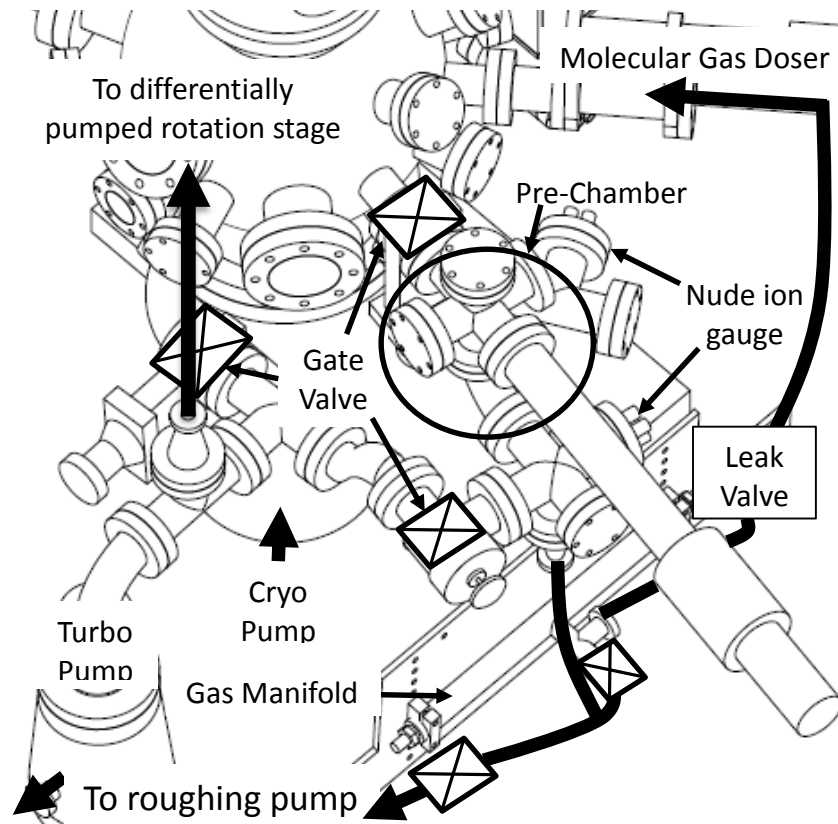
Figure 4: Chamber pumping scheme showing how pumping of multiple chamber sections can be accomplished. A single turbo pump is used to pump the main chamber to high vacuum, to pump the pre-chamber during sample introduction, and to pump the gas manifold to high vacuum pressures.

3.1.2   Sample holder, cooling, and manipulation

The position and alignment of the sample is controlled by a three axis translation stage (±12.5 mm range in the two horizontal directions and 100 mm range in the vertical) and a differentially pumped 360˚ rotation stage mounted on the top 8 in. port of the chamber (McCallister Tech). The cryogenic cold head and utility flange for electrical connections to vacuum are connected to the rotation stage (SHI-4-5 UHV, Janis Scientific). The cold head consists of a primary stage capable of reaching temperatures of <7 K and a gold-coated radiation shield that is held at ~35 K meant to deflect thermal radiation from the room temperature chamber walls. A custom designed dual sample holder is attached to the bottom of the primary stage and electrically isolated from the grounded main chamber by several sapphire washers. The sample holder consists of a QCM installed in the upper section, and molybdenum spring clips installed in the lower section hold the transferable sample flag securely against the sample holder to maximize thermal conductance. A Faraday cup is attached at the bottom of the sample holder to measure beam current at the sample irradiation position. The sample transfer system (VG Scienta), coupled to the pre-chamber on an equatorial chamber port, is used to transfer vertically mounted samples into and out of vacuum rapidly and without exposing the main chamber to atmosphere (Figure 5). It consists of a mechanical jaw that could be opened and closed in vacuum as well as horizontally translated from the pre-chamber to the main sample holder via magnetic coupling (Figure 6). Samples are mounted to the molybdenum transfer flag using either sample clips or a 90% transmittance Ni wire

grid. Samples held in the mechanical jaw can be baked under vacuum (~1x10^{-6} Torr) at ~200 C by wrapping the pre-chamber with resistive heating tapes. The radiation shield has machined holes precisely located to allow for the analysis and radiation of the samples, ion beam current measurement at the Faraday up, 0-90° access for the gas doser and mechanical jaw access during sample flag transfer.

Cryogenic cold head and utility flange for sample holder electrical connections

Pre-chamber (P_{min}~1x10^{-6})

XYZ-translation stage and 360˚ differentially pumped rotation stage to sample positioning

Magnetically coupled transfer arm and jaw

Main chamber body

Turbo molecular pump and oil free backing pump

Cryogenic pump and gate valve
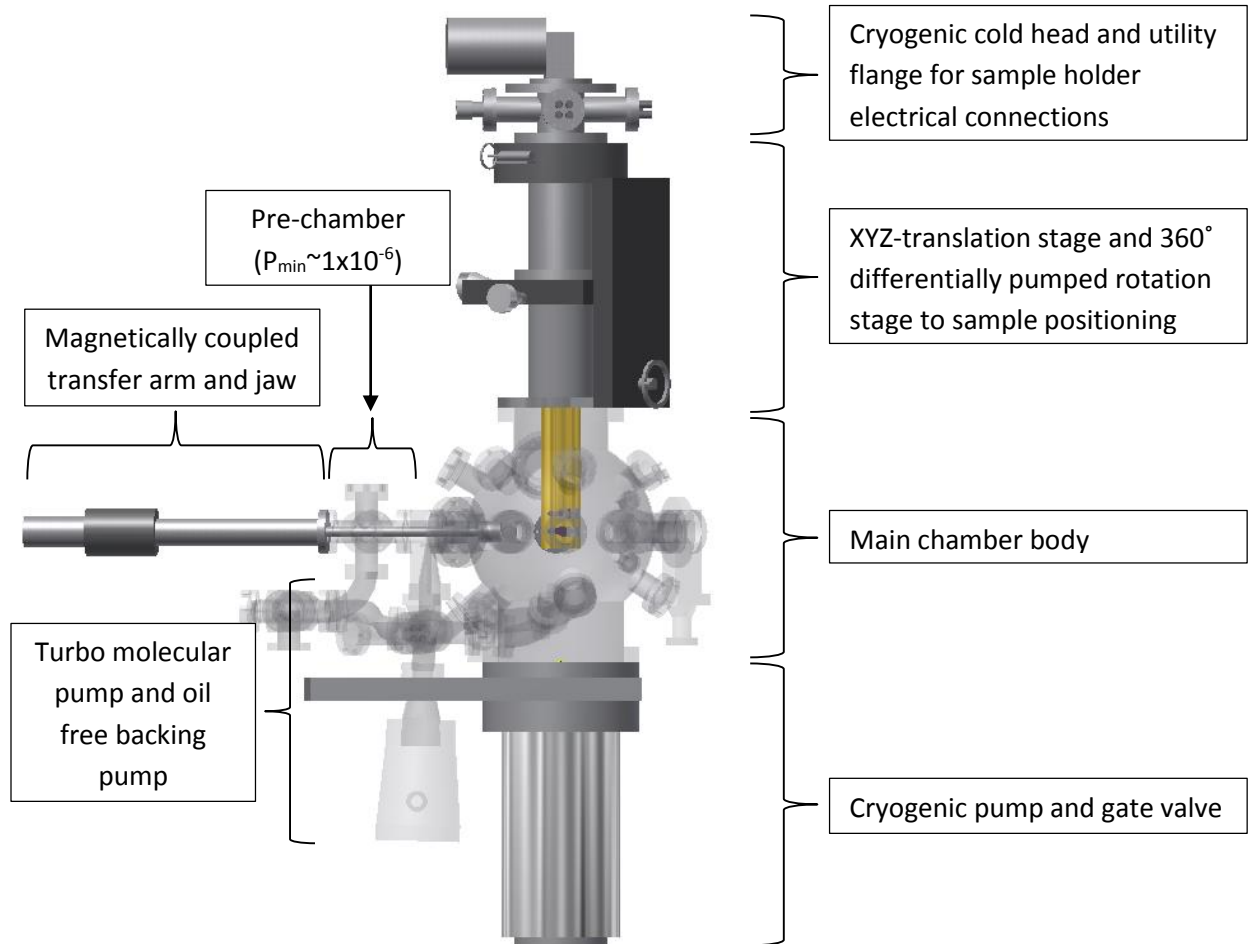
Figure 5: Main chamber features and transfer system. The cold head is connected to an external helium compressor and both the rotation stage and the pre-chamber are pumped by a 30 L/s turbo molecular pump.

Mechanical jaw opens and closes through magnetic coupling

Transfer flag held against sample holder using molybdenum clips
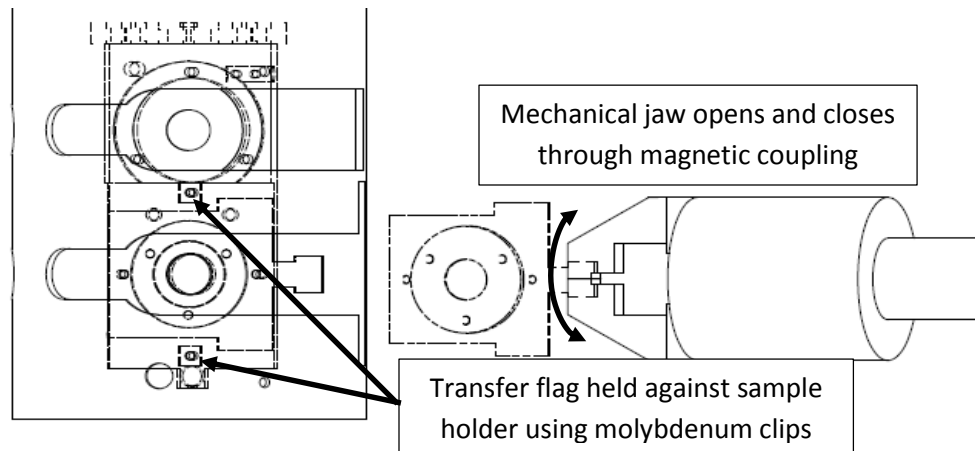
Figure 6: The transfer arm consists of a mechanical jaw which is activated though magnetically coupling. The transfer flag is held against the sample holder using two molybdenum clips and can reach temperatures as low as 15 K under full cooling power.

The sample holder was custom designed and fabricated from oxygen free high purity copper (OFHC) at the University of Virginia (Figure 7). The design incorporates elements from previous systems used in the LASP, as well as several novel features that have since been incorporated into subsequent instrument designs, thus proving their utility. Temperature is monitored by multiple Lakeshore Si diodes, capable of accurately measuring temperature to a precision of 0.01 K, with one diode installed in the primary stage of the cold head, another embedded in the sample holder and in contact with the QCM holder, and a third at the bottom of the radiation shield. The minimum temperature achieved at the sample holder is <7 K, and higher temperatures are maintained using two resistive heaters installed symmetrically on the back of the sample holder and an additional 50 W heater at the end of the primary stage connection. The sample holder is connected to the cold head primary stage using 6 stainless steel screws and electrically isolated using a sapphire disk between the cold head and sample holder surfaces and sapphire washers around each of the screws to keep them from making contact with the sample holder. A Faraday cup (FC) consisting of two electrically isolated plates and a 5mm long aluminum tube is installed at the bottom of the sample holder and can be positioned to accurately determine the current at the sample irradiation position. The front plate is used for locating and rough tuning the ion beam and contains a 1mm aperture that allows for precise measurements of beam flux (current/area) at the FC. The back plate can be negatively biased to suppress secondary electron emission from ions impacting the FC. The FC itself is a 2mm diameter aluminum tube from which an electrical connection is made with a Keithley electrometer capable of measuring current with a precision of <1 pA.

	Sapphire disk and washers between primary stage and sample holder for electrical isolation (not shown)
	Primary stage connection to Janis cold head. Si diode and 50 W heater embedded in flange (not shown)
	Si diode embedded in the sample holder and in contact with the QCM holder
	Quartz Crystal Microbalance (QCM) and connection to external oscillator circuit
	Transferable sample flag for vertically mounted sample
	Faraday cup (FC) and electrical connection to external electrometer (not shown)
	Negatively biased FC back plate for secondary electron suppression
	FC front plate with 1 mm aperture for precise beam flux measurement

Figure 7: Custom designed sample holder with major design features labeled.

3.1.3   Molecular Gas Doser

In order to deposit high purity ice films onto the sample holder, a molecular gas doser was custom designed and fabricated from stainless steel tubing and connected through a high precision leak valve to a gas manifold. Bottles of high purity gas and water ampules can be connected to the manifold and leaked at a controlled rate into the doser. As the gas passes through the doser tubing it is split between upper and lower paths, then moves into the doser tips where it first passes through a baffle and is then collimated into a parallel stream by passing it through a 0.5 mm thick glass microcapillary arrays consisting of numerous 10 µm diameter pores (Photonis). The doser is mounted on a linear translator and can be positioned from 50 mm to 5 mm from the sample substrate and, by turning the sample holder, gases can be deposited at angles from 0˚ to 90˚. The design allows films to be simultaneously deposited on the QCM and the mineral or glass substrates mounted on the transfer flag. Using the QCM for real-time monitoring of the deposited mass, ices of known thicknesses can be grown on the mineral samples. The thickness on the mineral substrates is measured using FTIR spectroscopy and deviations from the mass deposited on the QCM are indicative of differences in sticking probability of the gas species or temperature differences between the gold coated crystal and the mineral surface.

Welded and metal sealed connections to eliminate background gas leakage

From gas manifold

Doser can be positioned from 50 to 5 mm from the sample holder

The baffle diffuses the gas evenly throughout the doser tip and the microcapillary array collimates the molecular beam
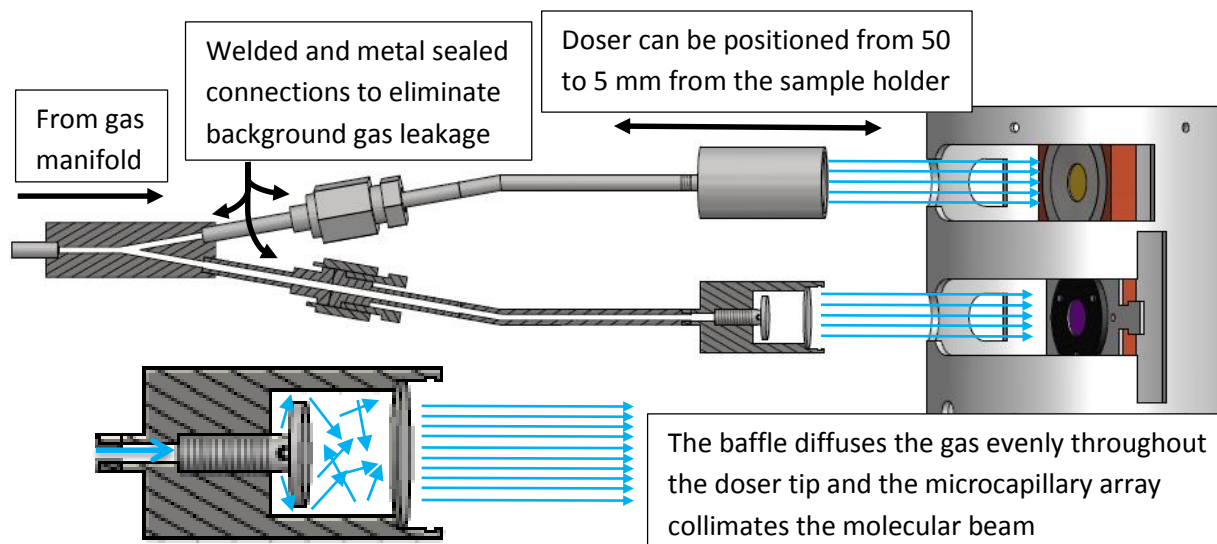
Figure 8: Dual molecular gas doser capable of simultaneously depositing high purity gases on the quartz crystal microbalance and mineral samples. The lower line of the doser is shown as a slice and the function of the baffle and microcapillary array is shown in detail in the lower left.

3.2 System performance testing

To verify the functionality of all equipment, several tests were carried out on the cooling and warming of the sample holder, ice deposition and desorption, beam current and sputtering of argon. The data collection for the experiments was accomplished by a LabView program based off of legacy programs and modified to communicate with the system instrument controllers through standard computer data transfer ports. The program was able to simultaneously collect temperature, pressure, gas partial pressure, ion beam current and QCM response and save the data to a file. Additionally, the program was integrated with the FTIR data collection software so that this information could be included in the spectra collection metadata. The computer could be accessed through remote connection software so that experimental parameters such as temperature and FTIR spectral collection settings could be changed and data collected without the operator being present. However, all sample positioning, beam irradiation, and gas deposition operations required manual operation.

3.2.1 Sample cooling

To test the thermal conductance between the sample holder and the transfer flag and determine the minimum temperature that could be reached for a mineral or glass sample, a Si-diode was temporarily installed on the transfer flag and the system cooled at a controlled rate while monitoring temperature on both the sample holder and transfer flag. It was found that although the flag and the sample holder cooled at approximately the same rate (Figure 9 A), the lowest temperature for the flag remained ~7 K above the sample holder at maximum cooling power (Figure 9 A inset). Warming the system at controlled rates of 0.5, 1, 2, and 3 K/min produced roughly identical temperature differences between the sample holder and transfer flag below ~50 K. However, at higher temperatures, the warming rate had a significant effect on how closely the transfer flag temperature tracked the sample holder, with faster rates producing a larger deviation as shown by taking a ratio of the temperatures (Figure 9 B). The ability to programmatically control the heating and cooling rates of the

sample holder allow for Temperature Programmed Desorption (TPD) measurements to be carried out. The TPD measurements require the combination of the QMS to monitor gas partial pressure while the sample is warming, and combining the pressure signal with the QCM response allows the temperature at which an ice film or surface species desorbs from the sample holder to be verified. An example of this sort of measurement is shown below (Figure 10)
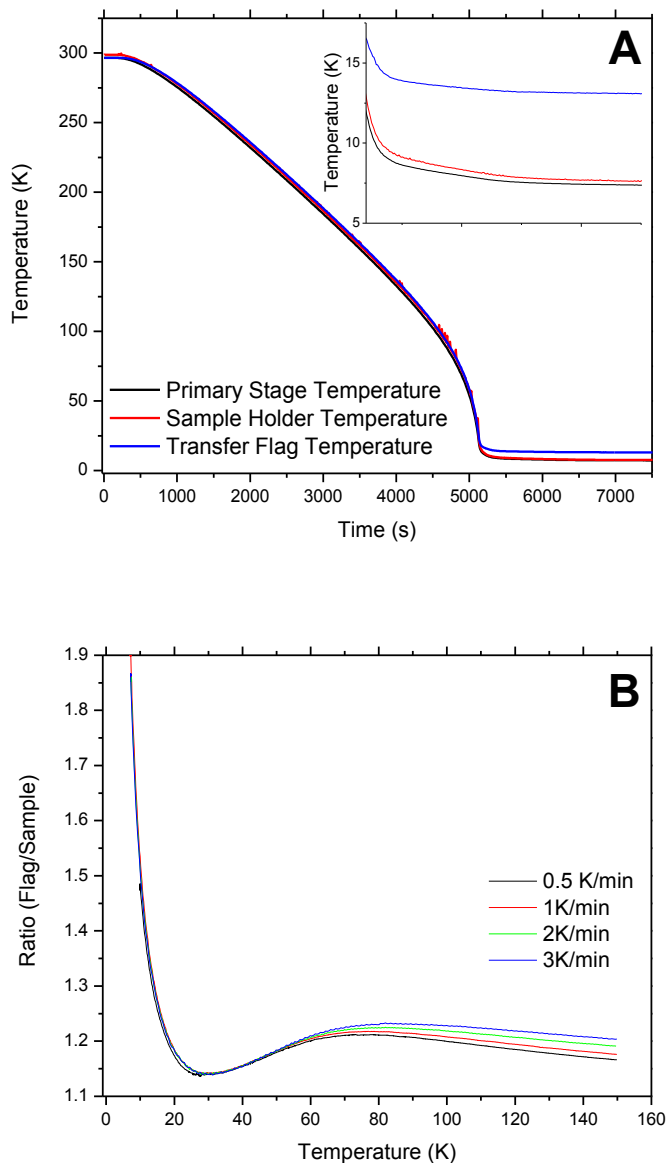
Figure 9: Cooling performance of the sample holder and the transfer flag. (A) The lowest temperature achieved by the transfer flag was ~10 K greater than the sample holder. (B) The rate at which the sample holder was warmed had little effect at temperatures <50 K but above that point the transfer flag temperature lagged behind the sample holder more the faster the warming rate.

3.2.2 Quartz crystal microbalance

The QCM is a gold coated quartz piezoelectric crystal with a fundamental resonance frequency of ~5.9 MHz. The crystal is driven at its resonance frequency by supplying an alternating voltage from an external oscillator circuit to the back electrode, and the resonance frequency is monitored by a Leybold Inficon XTC controller. The front electrode of the QCM (gold coated surface) is in electrical contact with the sample holder and can be used to monitor beam current during irradiation experiments. The alternating voltage used to drive resonance is applied to the back electrode which is electrically isolated from the sample holder by a ceramic cap. The resonance frequency of the crystal shifts as mass is deposited on the surface and, for small frequency shifts Δf relative to the fundamental frequency, the two can be related by the Saurbrey equation

$$\frac{\Delta m}{A} = \eta = -\frac{\sqrt{\rho_Q \mu_Q}}{2f_0} \Delta f = -s\Delta f$$

Equation 1

where η is the column density (mass per area) deposited over the 0.8 cm^2 active area at the center of the crystal, and s = $\frac{\sqrt{\rho_Q \mu_Q}}{2f_0}$ = 1.227x10^{-8} g s cm^{-2} is a constant related to the density (ρ_Q), shear modulus (μ_Q), and fundamental frequency (f_0) of the quartz crystal.

To test the operation of the QCM, the sample holder was cooled to 15 K and a film of pure argon was deposited to a measured column density of ~7x10^{-5} g/cm^2 which, for an argon density of 1.764 g/cm^3 [Grosjean, 1996], corresponds to a thickness of ~40 μm. The system was then warmed at a controlled rate of 1 K/min while monitoring the frequency of the crystal and the composition of background gases in the chamber using the Dycor QMS. Films can be deposited simultaneously onto the QCM and mineral or glass substrates mounted on the transfer flag, permitting measurements of desorption energies and sticking probabilities on a variety of surfaces; the QCM is used to monitor the thickness of the deposited film in real time while thicknesses grown on the mineral substrate can be verified using FTIR spectroscopy [Figure 10]. The graph below shows a large peak in Ar background pressure precisely at the same temperature where the mass present on the QCM drops to a minimum, giving complimentary indications that the Ar desorbs at a temperature of ~38 K, while peaks at higher temperatures in the QCM signal are due to residual desorption from further above on the the cold head second stage which warms more slowly than the sample holder.
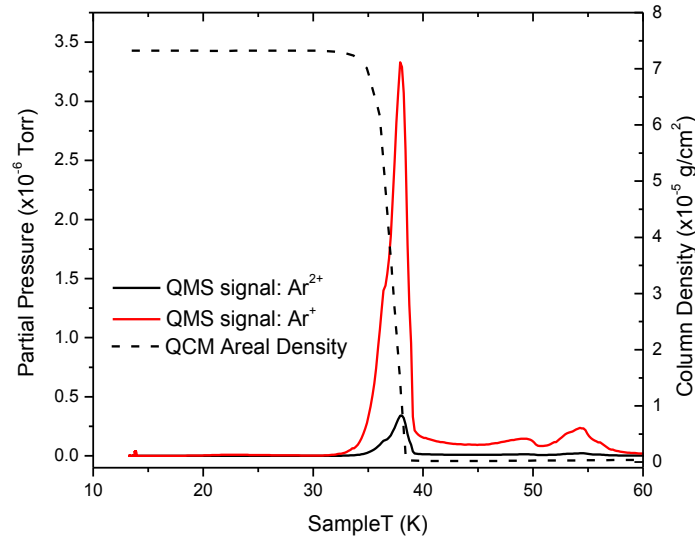
Figure 10: TPD measurements of argon ice grown on the QCM. The Ar partial pressure increased sharply as the sample holder temperature reached ~32 K and peaked at ~38 K, identical to the temperature at which the QCM signal dropped to zero mass deposited.

3.2.3 Ion accelerator

The accelerator consists of a duo-plasmatron ion source, acceleration stage, two symmetrical einzel lenses for beam focusing, a velocity filter for separating out specific ions, and a deflection region for beam positioning and rastering (Figure 11). Ionization is accomplished by passing a current through a tungsten filament, heating it to the point where electrons are emitted, and then accelerating the electrons by maintaining a ~100 V potential difference between the filament and the source region walls. The source pressure is held at ~100 mTorr and electron impacts with the gas produce bond breaking and ionization (electron impact ionization) of the gas atoms. A solenoid produced magnetic field causes the electrons to spiral around field lines, thus increasing their probability of collision with a gas molecule, producing a dense plasma near the source aperture. The plasma expands though the aperture and is then accelerated through the extraction gap at a determined energy in the range of 1-25 keV. The source was capable of producing an ion density sufficient to provide and a steady flux of >1x10^{12} ions cm^{-2} s^{-1}, measured at the sample holder, for all gases relevant to solar wind studies. As the energetic ionization process creates atoms and molecules of varying charge state (i.e. H_2^+, H^+, and He^{2+} depending on the source gas), the Wien filter is used to select ions of a specific charge to mass ratio to be directed on to the sample. The filter uses crossed electric and magnetic fields to impart acceleration to the ions, and by fine tuning of the electric field strength the acceleration of a given charge to mass ratio can be set to zero allowing the particle to pass through the filter region unaffected.

$$\bar{a} = \frac{q}{m}\left(\bar{E} + \bar{v} \times \bar{B}\right)$$
                                                                        Equation 2

where $\bar{a}$ is the acceleration, q is the ion charge, m is the ion mass, $\bar{E}$ is the tunable electric field, $\bar{v}$ is the ion velocity dependent on the acceleration voltage, and $\bar{B}$ is a constant magnetic field. The ability of the

Wien filter to select a specific mass to charge function is shown for several types of ions in Figure 12. A DC voltage applied to deflection plates in the region of the beam nearest the chamber is used to position the beam at the sample position, and a variable AC signal overlaid on the DC rasters the beam so that it is uniform across the entire sample area. In addition, a 1.5˚ bend is incorporated into the beamline to remove neutral species. The accelerator is differentially pumped by turbo molecular pumps at two different positions along its length, and the contribution of H_2 gas to the chamber pressure is ~1.5×10^{-9} Torr during irradiation. The sample positioning system allows 2-D beam profiles to be obtained at a resolution of ~1 mm and a typical beam pattern is shown in Figure 13.
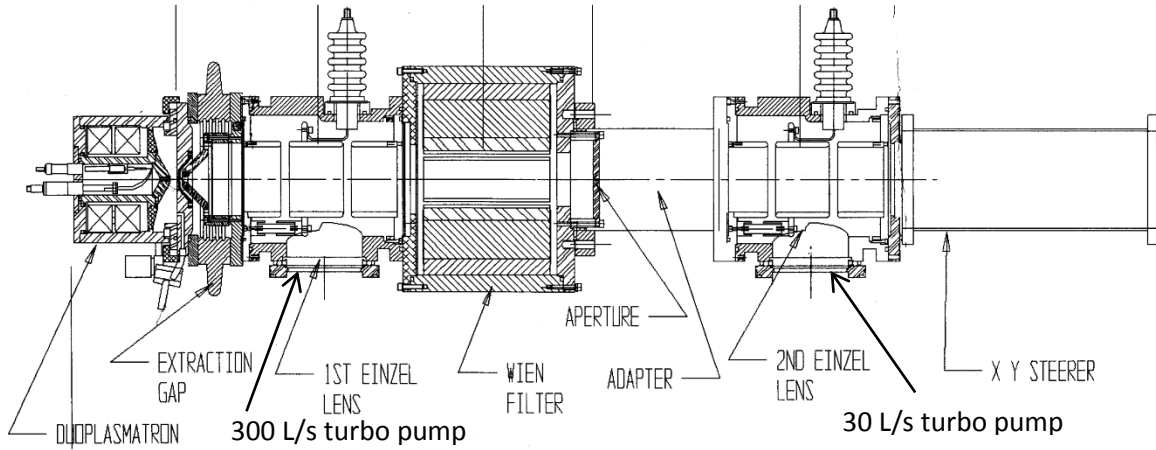
Figure 11: Schematic of the ion accelerator showing the ionizer and optical components for beam focusing and positioning. Image from Peabody Scientific.
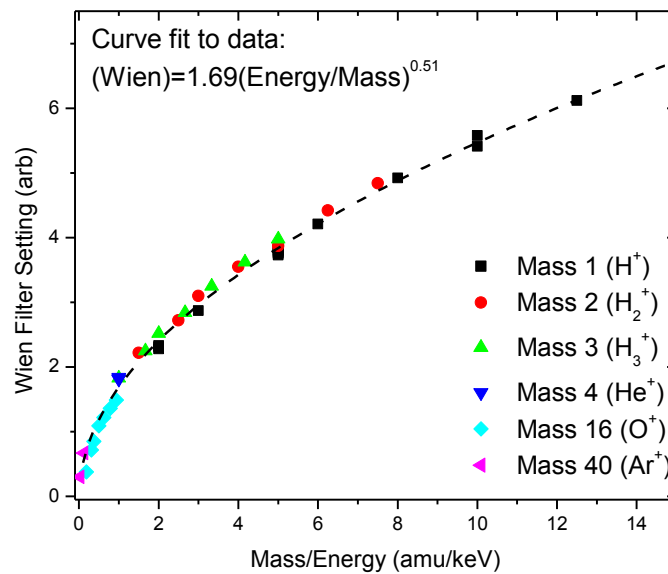
Figure 12: Plot of the Wien filter tunable electric field as a function of acceleration energy over ion mass. Data were collected for H^+, H_2^+, H_3^+, He^+, O^+, and Ar^+ ions and could be fit by a single curve.
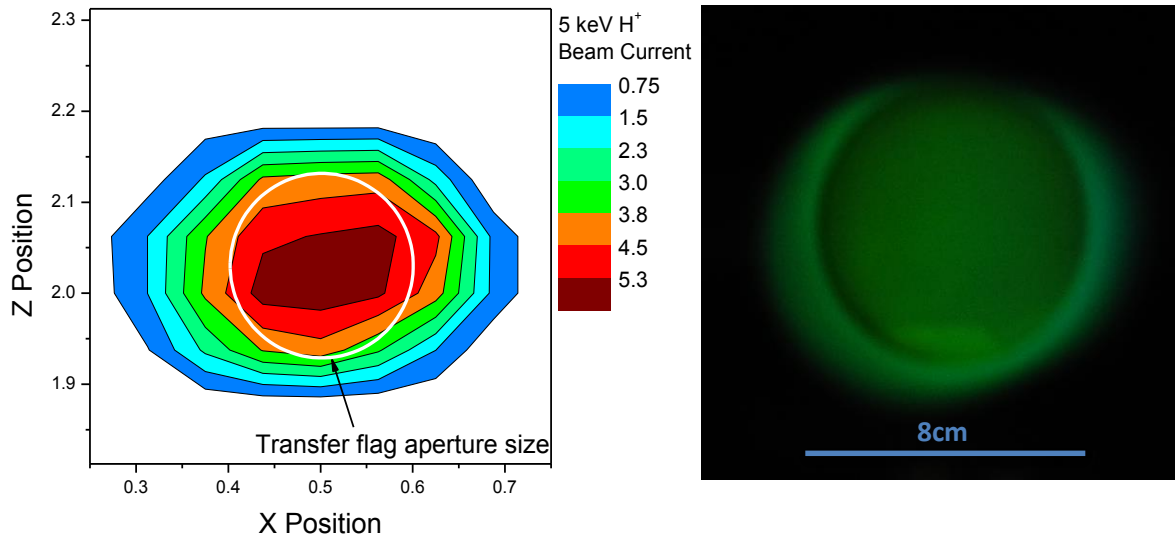
Figure 13: Typical 2-D beam profile for H⁺ is shown on the left. Current was measured at the faraday cup for a 5 keV H⁺ beam, and the decrease in beam current from the maximum at the center to the extent of the IR beam sensitive area is ~1.5 nA (~25%). The image on the right is luminescing argon on the QCM showing the beam size and uniformity.

As a test of the QCM and SIMS operation, Ar films were grown on the QCM and sputter removed using 5 keV H⁺ ions. Measurements of argon sputtering rates at energies from 10 to 50 keV have been made previously (Grosjean, 1996), and using linear extrapolation of the lowest energy measurements presented there (10 keV and 20 keV), the sputtering yield for 5 keV H⁺ ions was estimated to be ~21 Ar/H⁺. Comparison with these measurements was accomplished by irradiating an Ar film grown on the QCM with a rastered beam which yielded a sputtering rate of 18.1(±0.03) Ar/H⁺, slightly lower than the estimated value, although differences in temperature and irradiation angle between the measurements were not accounted for (Figure 14). Additionally, SIMS spectra were taken while irradiating an argon ice with deuterium ions and the spectra show both reflected D⁺ and sputtered Ar⁺ and Ar²⁺. The two SIMS spectra (lower graph) show argon ice irradiated normal to the surface and at 30˚ to the normal. The SIMS signal for the ice irradiated at an angle is larger than the normally irradiated film, although whether this was due to an increased sputtering yield expected for irradiation at angles deviating from normal or due to more sputtered ions reaching the SIMS detector because of the favorable detection geometry was not determined.

$$\eta_{mass} = -5.7 \times 10^{-7} - 1.2 \times 10^{-21} * \text{Fluence}$$
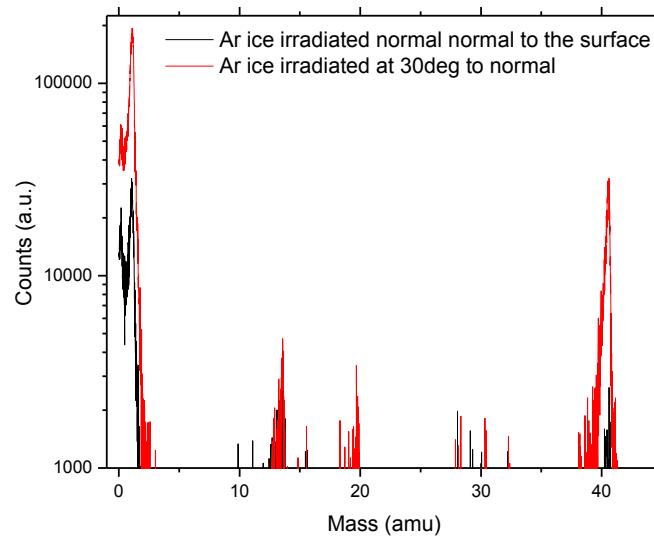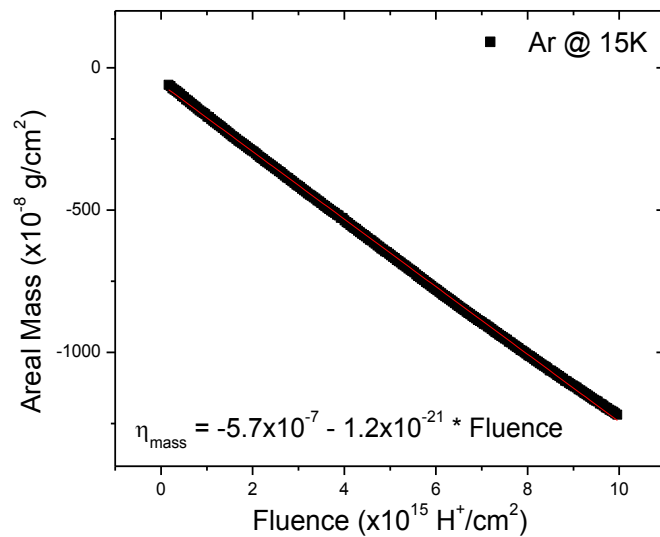
Figure 14: (Upper) Sputter removal of an Ar ice at 15 K from the QCM by a rastered beam of 5 keV H⁺ ions. The sputtering rate is found from the slope of the curve. The ice was irradiated at normal incidence and the beam uniformity across the crystal area deviated by no more than 25%. (Lower) SIMS spectra obtained during 5 keV D⁺ irradiation of argon ice as a function of irradiation angle. The Ice irradiated at 30˚ to the normal has a larger yield, as detected by SIMS, than the ice irradiated normal to the surface.

3.2.4 FTIR Spectroscopy

Minerals are analyzed using FTIR spectroscopy (Nexus 670, Thermo-Nicolet) which could be arranged in either reflectance or transmission mode. Transmission through the sample holder is limited by a 5 mm hole in the transfer flag which works as an aperture to constrain the analysis area to only the irradiated region. Between irradiation and transmission IR measurements, the sample must be rotated

50˚. In order to ensure that the sample area analyzed by FTIR was the same as that being irradiated the beams were simultaneously aligned by first growing an Ar film (~2 µm thick) on the transfer flag using the dual-tip doser and irradiating it using keV H^+ ions, causing it to luminesce (Grosjean, 1996). While the film was luminescing, the FTIR beam was positioned over the aperture in the transfer flag such that the signal strength at the detector was maximized (Figure 15). The sample coordinates were then noted and subsequent irradiations and IR analyses were taken at the same position. This alignment was performed approximately every 6 months or after configuration changes were made to the sample holder.
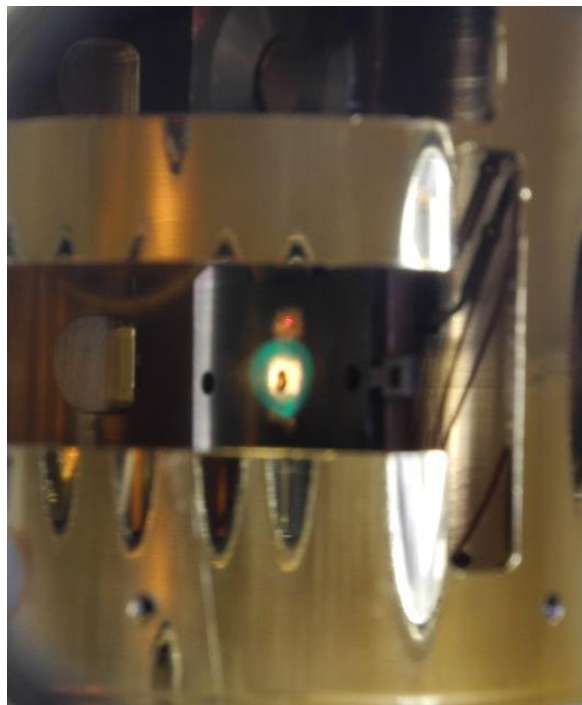
Figure 15: The ion beam and FTIR beam were aligned so that the sensitive area of the IR was covering the same region that was irradiated. The upper and lower light spots are due to multiple reflections in the spectrometer and did not contribute to the FTIR signal.

FTIR spectra were taken using both white light halogen (25000-5000 cm^{-1}) and infrared glo-bar (9000-50 cm^{-1}) sources and Mercury-Cadmium-Telluride (MCT), Indium-Gallium-Arsenide (InGaAs), or Dueterated TriGlycine Sulfate (DTGS) detectors sensitive to a total wavelength range from 0.9 to 20 um. Spectra can be taken both inside the spectrometer bench and within the UHV chamber. A series of gold coated mirrors (II-VI Infrared, Edwards Optics) are used to to focus and collect the light from the sample and redirect it to the detector, and an internal mirror redirects the light from the spectrometer bench to the chamber sample holder. The beam path after it leaves the spectrometer is shown in Figure 3. The amount of light incident on the sample can be changed using an adjustable aperture at the light source, and the minimum beam spot in the chamber is ~3mm diameter (size = 1). The beam intensity was greatest at the center of the beam spot and the total signal increases at larger aperture sizes. However, the increase was slight for size settings greater than '4' indicating the beam size was ~5mm at that setting, equal to the transfer flag aperture size. The windows used to admit the light into the chamber

were KBr with a transmittance range from 25000 to 500 cm^{-1}. The external optics and detector were contained in sealed aluminum boxes and continuously purged with dry air from which > 99% of the water vapor and CO_2, both of which contain infrared absorptions in the region of interest for these experiments, had been removed (Model #75-60, Parker Balston). The mineral samples analyzed were typically from 100-200 μm thick, causing the Si-O stretch bands near 10 μm to be fully absorbing and strong overtone absorptions at 5-6 μm to appear (Figure 16). The ability to cool the sample while simultaneously taking IR spectra allowed analysis of changes in the shape of the water absorption band, thereby determining the mode of incorporation (i.e. structurally bound, trapped in point defects or in inclusions) of water into the minerals (Aines and Rossman, 1984).
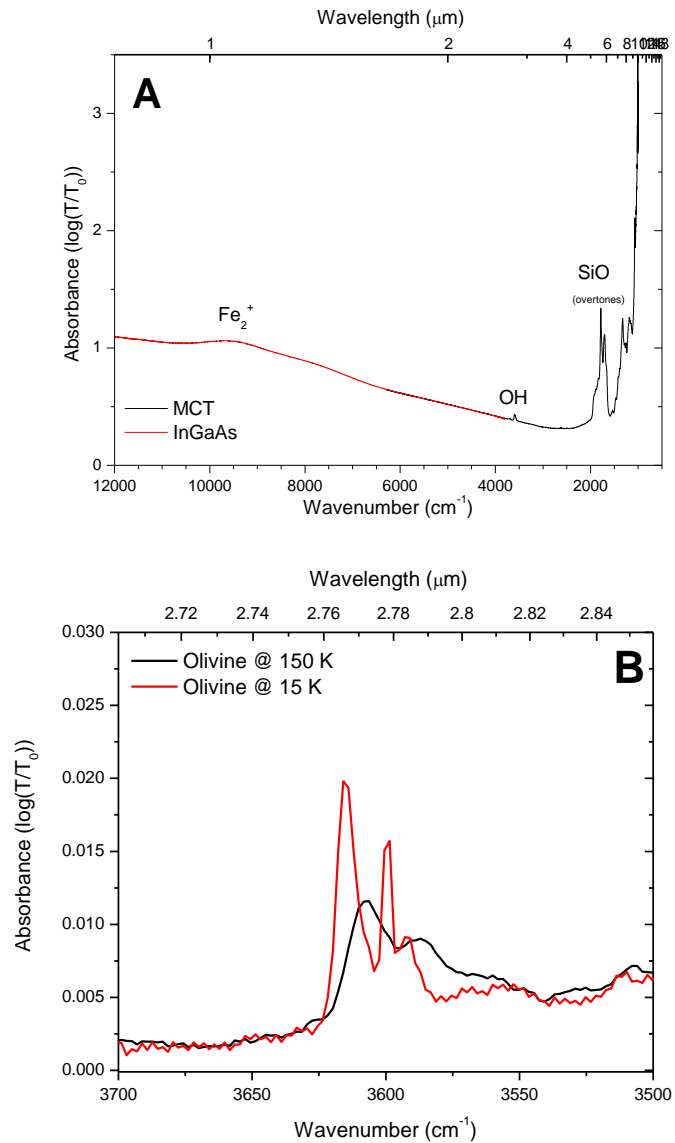
Figure 16: FTIR spectra of olivine. (A) Full spectra taken with InGaAs and MCT detectors showing crystal field splitting absorption due to Fe^{2+} transitions at 1um and SiO stretch overtones near 5.5 um. Absorptions above ~9μm (Si-O

4   Sputter removal of H_2O deposited on lunar soil

As a preliminary experiment, the sputtering cross-section for water vapor deposited on mature Apollo 16 lunar highland soil sample 65901 was measured for 4 keV He^+ irradiation. These analyses were performed under UHV (base pressure ~10-9 Torr) in a second vacuum chamber, a Physical Electronics 560 XPS/SAM system, equipped with an X-ray Photoelectron Spectrometer (XPS), a low energy ion gun (Perkin Elmer), a LN2 cooled sample holder, a SIMS (Hiden Analytical), and a high purity water doser. The XPS system consists of a dual anode X-ray source mounted perpendicular to the double-pass, cylindrical-mirror electron energy analyzer (CMA). XPS is a quantitative surface analytical technique that uses mono-energetic X-rays that penetrate the sample surface, ejecting inner shell electrons of a characteristic binding energy (BE) with respect to the Fermi level. These photoelectrons have a kinetic energy in the spectrometer, $E_x - BE - \Phi$, where Φ is the measured work function of the spectrometer and E_x is the energy of the incident x-ray. The kinetic energy of the photoelectrons serves to identify the element, and the intensities of the photoelectron peaks can be used to determine atomic abundances by comparing them to a calibration standard. The XPS signal is provided by those photoelectrons that leave the sample surface without energy loss, originating from a thin surface layer (2-4 nm on average, depending on the photoelectron energy). Elemental composition is obtained by incorporating the instrument sensitivity for each element, providing quantitative information with an accuracy of ~15%. The CMA was operated at an energy resolution of 3.2 eV to provide high sensitivity, ensuring that all the surface constituents of each mineral were accurately identified. Data were taken using primarily Al (Kα 1,2) X-rays to minimize the overlap of Auger and photoelectron spectra.

An XPS spectra of mature lunar soil sample 65901 is shown in Figure 17 and a comparison to published values given in Table 1. The composition values are given in atomic percentage of the surface and the results obtained in this study agree well with published values, with the exception of carbon. Reasons for the slight variation in the major species can be explained by different compositions for samples collected at different lunar sites, as well as differences between surface and bulk composition (Housley, 1992). Carbon in the analysis is due to unavoidable atmospheric contamination at the surface of the soil grains. The bulk values taken from the lunar sample compendium were determined with Instrumental Neutron Activation Analysis (INAA) which is insensitive to the surface composition (Laul and Schmitt, 1973), whereas the XPS analysis of Housley, while mentioning the presence of carbon, assumes it is entirely due to contamination and ignores its contribution in the final atomic composition (Housley and Grant, 1976). Although the samples in the current experiments were sputter cleaned prior to analysis, the ion irradiation angle was different than that of the electron analyzer and the sample could not be tilted past several degree from horizontal due to the risk of loose powder cascading and falling from the sample holder. Thus, due to the granular nature of the soil, part of the surface seen during XPS analysis had not been sputter cleaned and thus there was a residual carbon content in the final atomic composition. The same shadowing effects were seen after dosing the samples with water.
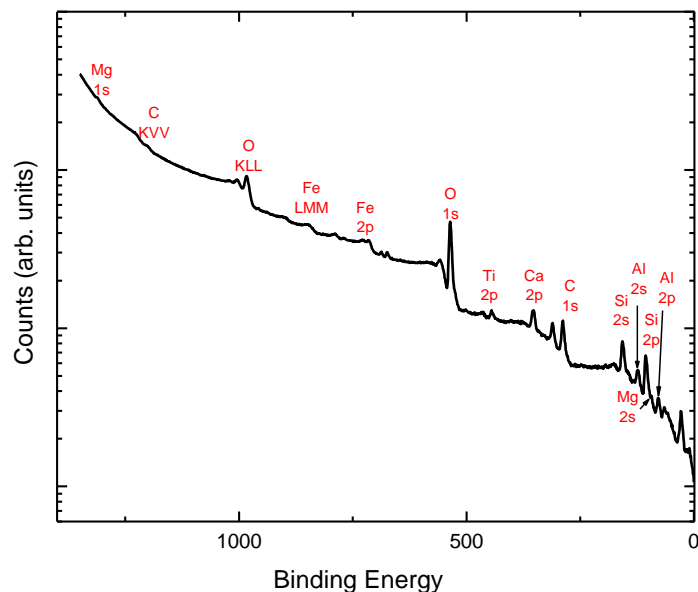
Figure 17: XPS spectrum of lunar soil sample 65901 taken with Al-K X-rays. The C peak in the spectrum is due to atmospheric hydrocarbon contamination and can be partially removed by ion sputtering. The peak heights can be related to atomic percentages using tabulated sensitivities in standard software.

Table 1: Elemental composition in atomic percent determined by XPS taken from Housley (1992) and measured in this work, and comparison to composition values found in the lunar sample compendium.

Sample	Si	Mg	Al	Fe	Ca	O	C
65701 - Surface (XPS) (FROM HOUSLEY, 1992)	18.5	2.1	9.4	3.1	5.3	61.6	
65901 - Bulk (INAA) Lunar sample compendium	16.6	3.4	11.3	1.8	5.9	60.7	
65901- Surface (XPS) This work	12.3	3.3	9.2	1.8	5.0	56.6	11.8

In these experiments, a small (~0.1 g) sample of lunar soil was deposited in a 10 mm diameter x 1 mm deep copper cup and placed on a LN$_2$-cooled sample holder (Figure 18). The soil was neither compressed nor held with a bonding agent such as carbon tape, thereby closely simulating the lunar surface. Before water growth, adventitious carbon and atmospheric water were removed from the grain surfaces by irradiating the sample using 1 keV Xe$^+$ ions to a fluence of 2x10^{16} ions cm^{-2}. Low energy xenon was used to minimize the damage to the rims on the lunar soil grains and limit layer mixing. The removal of the atmospheric species was identified with XPS as a decrease in the atomic percentage of carbon present on the surface and in the oxygen to silicon ratio. The sample was then cooled to ~ 80 K

and dosed with water at normal incidence through a microcapillary array. The water deposited was thermally stable during the experiments at 120 K and desorbed completely at 180 K.
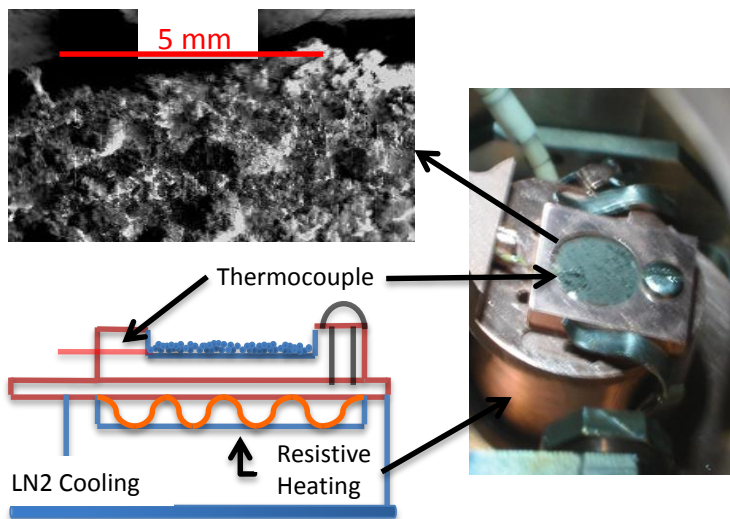
Figure 18: Sample setup during water sputtering experiments. The sample was cooled using an externally connected liquid nitrogen Dewar and temperature monitored using a thermocouple in contact with the lunar soil. The image in the upper left shows a SEM image of the sample in situ. The ion beam was rastered to cover the entire sample.

The amount of water deposited on the soil was determined by the increase in atomic percentage of oxygen on the surface relative to the concentration of the native soil species (Si, Ca, etc.). The soil was irradiated with 4 keV He^+ ions rastered uniformly over an area larger than that sampled by XPS. The ion beam was positioned at an angle of 25.3° to the surface normal, but the roughness of the soil means that the local incidence angles varied with position on the granular surface. Irradiation was done at a flux of ~10^{14} ions cm^{-2} s^{-1}, as measured with a Faraday cup. XPS measurements were taken at determined fluence intervals during the irradiation in order to quantify the amount of water remaining on the soil. Irradiation was done at a flux of ~10^{14} ions cm^{-2} s^{-1}, as measured with a Faraday cup. This flux is seven orders of magnitude larger than at the Moon but, at 0.064-Watts cm-2, the power density is insufficient to cause detectable heating. In addition to the XPS measurements, a Hiden Quadrupole Mass Spectrometer positioned at an angle of 46.9° to the sample normal was used to monitor the negative sputtered ions during irradiation. In additions, the SIMS was used to determine a composition for the lunar sample by measuring the positive ion sputter products as well as the energy of the sputtered positive ions (Figure 19). The desorbed O^- and OH^- ions were taken using negative SIMS and the yield followed an exponential decrease with increasing ion fluence.
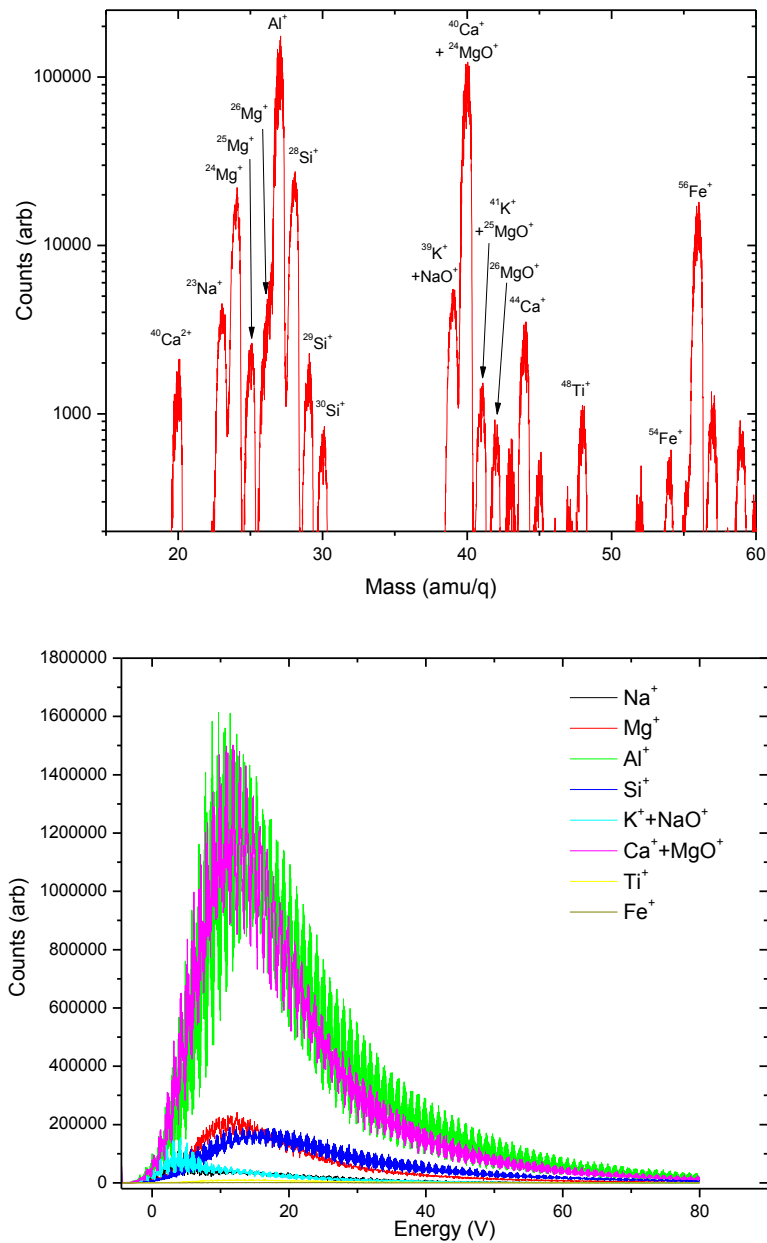
Figure 19: SIMS spectra taken during 4 keV He⁺ ion bombardment. (Upper) SIMS analysis of sputtered ions from lunar soil sample 65901 with major ion species labeled. The spectra can separate out the various isotopes of the ejected ions. (Lower) Ejected ion energies for the major composition species.

The increase in the ratio of O to Si due to water adsorption, measured by XPS, as a function of fluence (Figure 20) shows a complex behavior. Two exponential decays were fit to the data for different fluence regimes, giving cross sections σ_1 and σ_2 for the initial and final decay. These are interpreted to correspond to the removal of about a monolayer of water in the form of ice and a residual monolayer of water adsorbed on the soil. The cross-section of $\sigma_1 = 3(\pm1) \times 10^{-15}$ cm² and the column density of about one monolayer, or $\eta \sim 1 \times 10^{15}$ H₂O cm⁻², implies an initial sputtering yield $Y = \sigma_1\eta \sim 3$ H₂O/He, of the same order as the measured sputtering yield for ice (Famá et al. 2008). The second cross-section, $\sigma_{2 =}$

1.2(±0.4) x 10^{-16} cm^2, is interpreted as desorption of a tightly bound layer that remains adsorbed on the soil after the ice is removed. This type of behavior has been seen previously in the sputtering of Na from minerals (Dukes et al. 2011).
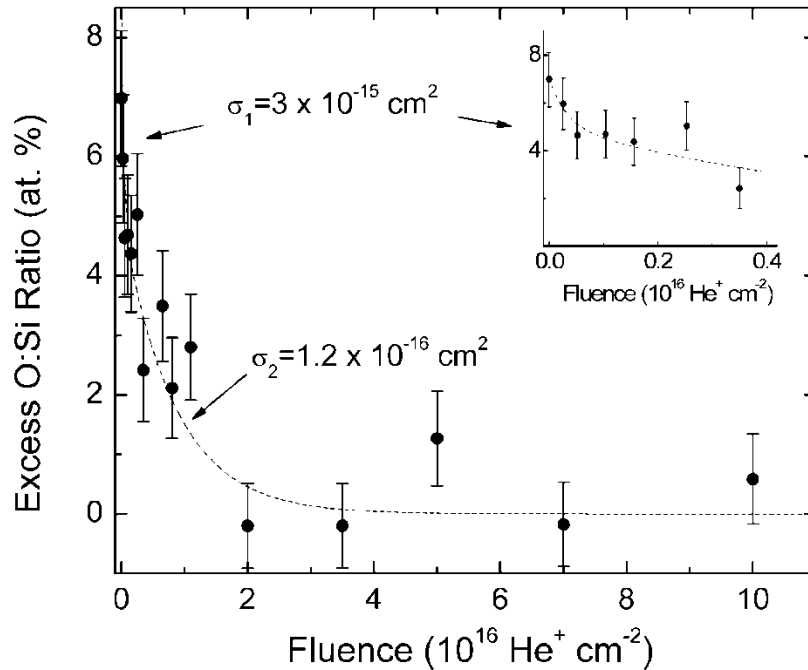
Figure 20: XPS measurements of the desorption curve of H$_2$O from lunar soil showing exponential decrease in the amount of oxygen on the sample surface. The data are fit by two exponentials representative of multilayer sputtering (σ_1) and sputtering of a single monolayer (σ_2).

In addition to the XPS measurements, sputtered water was monitored using SIMS in the negative ion configuration (Figure 21). The total counts of OH$^-$ and H$_2$O$^-$ were measured during each irradiation fluence and were found to decrease exponentially, similar to the XPS measurements. The cross-section was the same, within error, for both monitored species, and of the same order of magnitude as that measured by XPS. The explanation for the discrepancy in the measured cross-sections by XPS and SIMS was determined to be the size of the rastered irradiation beam and differences in the analysis angles of the instruments. The raster size was >10 mm meaning that some of the detected sputtered species were from the copper cup, and the area analyzed by XPS included regions of the grains that were shadowed from the ion irradiation.
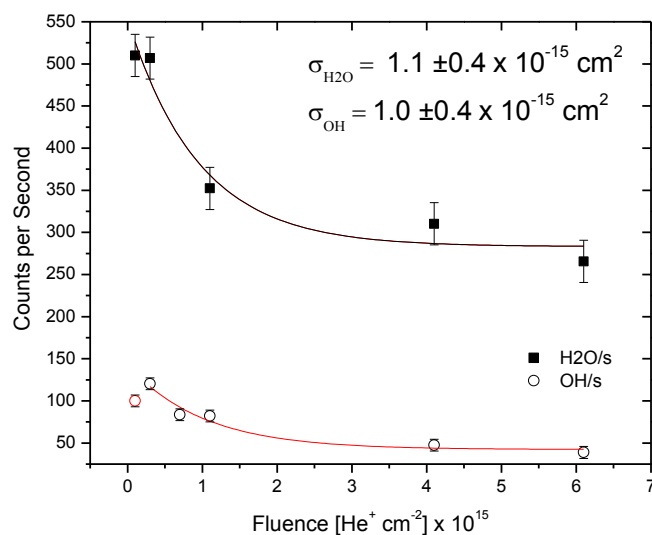
Figure 21: Sputtering cross-section measured using negative SIMS to detect ejected negative ions. The cross-section is similar to that measured using XPS, with differences being attributed to the raster size of the ion beam.

5 Ion implantation into minerals and a-SiO$_2$

Mineral samples were prepared using a precision saw with a diamond coated blade to cut sections <25 mm diameter and ~300 μm thick from larger pieces. The sections were then mounted on transparent microscope slides using Crystal bond^{TM} and reduced to their final thickness by sequential grinding with 320, 400, and 600 grit sandpaper (36 μm, 23 μm, and 16 μm average particle diameter respectively) on a water fed rotary polishing wheel. Using a micrometer to measure the thickness difference between the slide and the sample face, thicknesses ~150 μm could be accurately reproduced. Final sample thicknesses were accurately measured using a Hirox KH7700 stereo microscope at 3500x magnification by a digital measurement of the distance traveled by the microscope head between the focal plane at the sample surface and the sample holder.
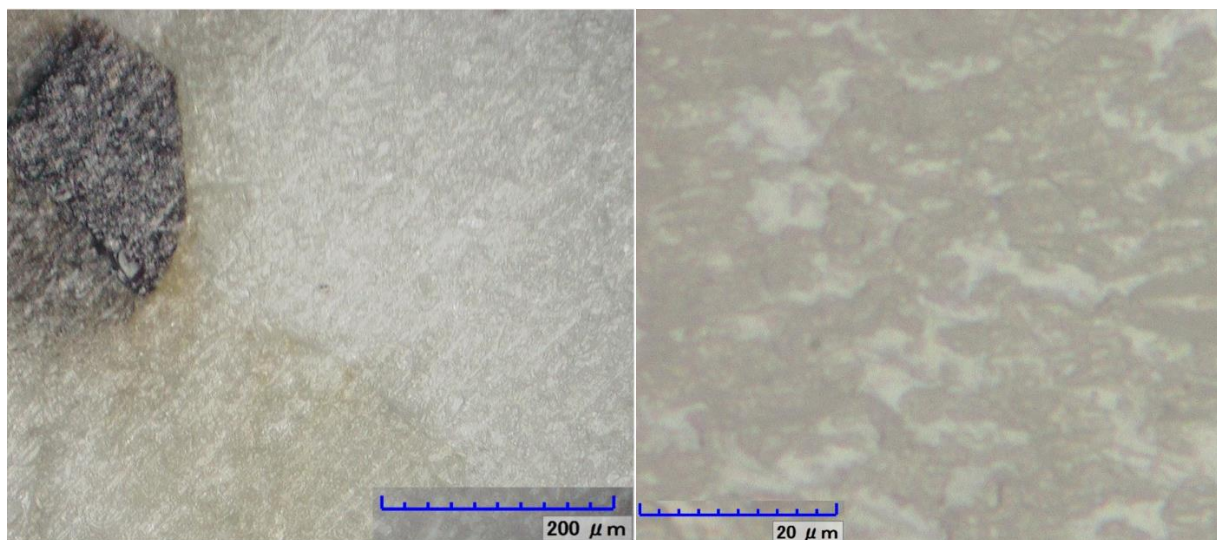
Figure 22: Stereomicroscope images of San Carlos olivine sample at (left) 350x and (right) 3500x magnification.

The adhesive used to bond samples to the preparation slides was removed by immersing them in solvents (acetone or isopropyl) and either allowing them to soak for up to 1 week to ensure all adhesive was dissolved or, for thicker samples, placing them in an ultrasonicator for 15 min while immersed in acetone, followed by 15 min in isopropyl. Samples were then rinsed using HPLC grade water and mounted to a transferable sample flag using 90% transparency Ni wire grid (70LPI, Precision E-forming) (Figure 23). In addition to securing the sample to the transfer flag, the use of the wire grid was meant to reduce surface charging during irradiation of insulating surfaces by providing accumulated charge a path to ground. For the samples analyzed, the only major absorption in the 2500-4500 cm^{-1} region was that due to the OH stretch absorption. The sample and mount were baked in vacuum at ~200 °C for 24 hrs to remove surface contaminants due to atmospheric exposure and then directly transferred to the analysis position without atmospheric exposure. Ion irradiations were performed in the UHV chamber at a base pressure of <1x10^{-9} Torr, with H$_2$ partial pressure during irradiation increasing to ~1.5x10^{-9} Torr. Performing the sample preparation and analysis entirely under vacuum conditions ensured that no water or atmospheric gases adsorbed on/diffused into the material or altered bonding between implanted hydrogen and structural atoms.
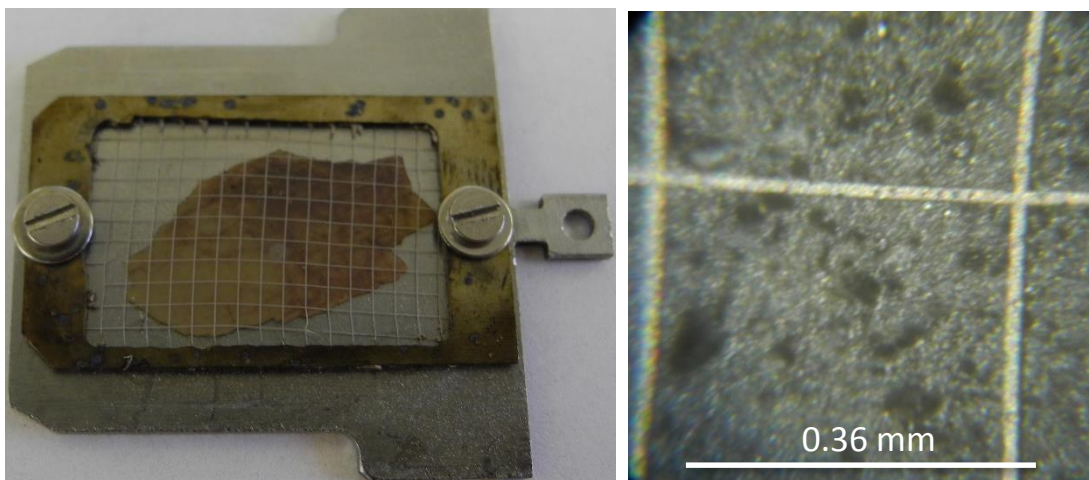
Figure 23: (Left) Olivine sample mounted secured to the transfer flag using a Ni wire grid. (Right) In situ image of the olivine sample taken using a high power optical telescope.

Samples were implanted with H^+, He^+, and Ar^+ ions at fluxes on the order of $\sim 5 \times 10^{12}$ cm^{-2} s^{-1}, meaning fluences of 2×10^{17} H^+/cm^2, equivalent to surface exposure times of ~ 40 years at the subsolar point or ~ 750 years at $80°$ latitude, could be reached in ~ 10 hours experiment time. The ion beam flux was measured at the Faraday cup through a 1 mm diameter aperture, and the fluence F of ions implanted into the sample was determined by integrating over the irradiation time. While these fluxes are larger than typical solar wind fluxes ($\sim 2 \times 10^8$ cm^{-2} s^{-1}), the power density is only $\sim 4 \times 10^{-3}$ Watts/cm^2 and causes temperature changes determined to be at most only a fraction of a degree during irradiation as measured by temperature sensors installed on the sample holder. Irradiations were performed at normal incidence with energies in the range of 2 - 5 keV, slightly higher than the average solar wind energy (~ 1 keV) but still within typical ranges. Previous experiments were done using 2 keV H_2^+ ions which were expected to split on contact with the surface with an equal amount of energy (1keV) partitioned to each atom [Burke, et al, 2011; Ichimura, et al, 2012]. In the current experiments, the use of a mass analyzed beam means that it is unnecessary to assume that the OH production is the same for protons (H^+) and two-correlated hydrogen (H_2^+). Several samples were first irradiated with an inert ion (He^+ or Ar^+) to determine the effect of radiation damage on the formation of OH. All samples were irradiated in sequences of increasing fluence, with typical fluences of $\sim 2 \times 10^{15}$ ion/cm^2 between acquired spectra, though the intervals between collected spectra were increased somewhat as the absorption bands neared the saturation limit.

The structural and/or chemical changes were monitored using FTIR spectroscopy, with an emphasis placed on the OH bonds formed due to irradiation. The infrared spectrometer was connected to the chamber through dry-air purged paths, and the beam was focused onto the sample using a gold coated, 375 mm focal length, $90°$ off-axis parabolic mirror. Light was collected by a second parabolic mirror (275 mm focal length) and focused onto a room temperature DTGS detector. The sensitivity of the FTIR measurements was $\sim 3 \times 10^{-4}$ absorbance in transmission, corresponding to $\sim 1 \times 10^{15}$ OH/cm^2. Using a room temperature DTGS detector eliminated uncertainty due to water condensed on LN2 cooled detectors as seen in previous studies [Theocharous, 2005; Burke et al, 2011]. Infrared spectra were taken from 5000-500 cm^{-1} at a resolution of 8 cm^{-1} and averaged over 1024 scans for a high signal

to noise ratio. By taking the spectral difference before and after irradiation the change in OH concentration resulting from H^{+} implantation could be distinguished from atmospheric and intrinsic (e.g. H_2O in inclusions) signals.

Though a proven technique in identifying water in minerals, quantitative FTIR spectroscopy requires calibration measurements on materials containing known concentrations of OH and water. The integrated molar absorption coefficients used to calculate column density were taken from published studies where OH concentrations were measured using more direct techniques such as ^{15}N nuclear reaction and dehydration weight loss [Bell et al, 2003; Davis et al, 1996].

5.1   Data Reduction

The infrared absorption depths are analyzed following the Beer-Lambert law which states

$$\frac{I}{I_0} = 10^{-\alpha'\ell} = e^{-\alpha\ell}$$
Equation 3

where I/I_o is the ratio of the intensities of the detected infrared beam after passing through the sample to that with the sample removed and α' is the decadal absorption coefficient often used in the geology literature and α is the natural log absorption coefficient most often used in physics and astronomy. Note that $\alpha \neq \alpha'$ and that the absorption coefficient is related to molar absorptivity ε by

$$\alpha = \varepsilon\, c$$
Equation 4

where c is the molar concentration of the absorbing species. The measurements of band depth and area (integrated over wavenumber) were taken after subtracting a quadratic baseline from the raw absorption spectra with the Omnic software. An advantage of the transmission IR setup vs. previous experiments is that the column density η of new OH bonds produced along the path of the protons can be directly quantified. The analysis proceeded by first lifting the sample holder clear and acquiring a background spectrum I_o with only the optics and KBr windows in the IR beam path. The sample was then lowered so that the IR beam was centered on the transfer flag aperture, and another spectrum taken. Absorbance, a dimensionless quantity hereafter given in terms of dimensionless absorbance units (a.u.), is calculated by taking the negative natural log or log base-10 of the ratio of the two spectra

$$A = -ln\left(\frac{I}{I_0}\right) = -log\left(\frac{I}{I_0}\right) * ln(10)$$
Equation 5

where I is the sample spectrum. For the irradiated samples, we likewise obtain A', and then the difference $\Delta A = A'-A$, which cancelled instrumental effects such as the presence of the wire grid in front of the sample. Then OH column density can be determined either from the height of the absorption band (BH) in ΔA and the molar absorption coefficient ε, or from the band area (BA) and the integrated molar absorption coefficient, ε_{int}. The column density is given by

$$\eta = \frac{BH \times N_A}{\varepsilon} = \frac{BA \times N_A}{\varepsilon_{int}}$$
Equation 6

Band height and area measurements were taken after using standard software to subtract smooth baselines from the absorption spectra A and A' so that there was a common basis from which to

measure the peak differences (height or band area). Subtraction was carried out the spectral range ±1000 cm^{-1} from the water band peak position so that the high absorbance Si-O bands, which are several orders of magnitude larger than the OH bands [Figure 16], did not affect the baseline. The subtraction procedure uses a quadratic line fit to the absorbance data $A(x)$ by least the least squares method.

$$A(x) \sim Y(X) = ax^2 + bx + c$$

Equation 7

The maximum difference between $A(x)$ and $Y(x)$ is then determined, and all points in the $A(x)$ that differ from the corresponding point in $Y(x)$ by more than half of this maximum value are dropped to create a subset of data with the tops of the major peaks missing. The same procedure – fit, compare, and drop – is then repeated for the subset, and the processes repeated 20 times. After the 20 iterations, the final subset $Y(x)$ is subtracted from the original spectrum $A(x)$ to produce the baseline corrected spectrum. Finally, the lowest point on the corrected spectrum is automatically set to zero.

One issue with using terrestrial minerals is that there is invariably residual water content that must be subtracted from the calculated amounts of OH formed by irradiation. For polycrystalline minerals, the residual signal could be due to H_2O contained in inclusions as well as structurally bound OH. Cooling the sample allowed molecular water to be distinguished from structurally bound OH as noted in Section 3.2.4 and discussed further below. The absorbance band of the olivine was broad and structureless, very different than previously published olivine spectra [Bell et al, 2003] though quite similar to absorptions for glassy silicate samples [Stolper, 1982; Paterson, 1982]. Paterson (1982) determined that the strength of the absorption coefficient depends on the peak wavenumber of the OH absorption band and developed a calibration relating the two. Libowitzky and Rossman (1996) pointed out that unpolarized measurements for crystalline minerals yielded unreliable estimates of the water contents, and this was further discussed for olivine by Bell et al. (2003) with direct comparisons being made to the Paterson calibration. However, the OH absorbance peak height for the olivine spectra of Bell et al. (2003) was several orders of magnitude higher than in the current experiments, and because the shape of the band found in the irradiated olivine was most similar to the absorption bands discussed for quartz by Paterson (1982), the calibration given there was used to determine the OH column density increase due to H$^+$ implantation:

$$\eta = N_A \int \frac{A(\nu)}{\gamma \, \varepsilon_{int,||}(\nu)} d\nu$$

Equation 8

where N_A is Avagadro's number, $A(\nu)$ is the measured absorbance, and γ is a polarization factor taken as 1/3 for amorphous materials (isotropic distribution of OH orientations in the material). The factor $\varepsilon_{int,||} = 150(3780-\nu)$ is the integrated molar absorption coefficient fit by Paterson for a variety of silica and silicate glasses. An effective integral molar absorption coefficient ε_{eff} can be calculated by:

$$\varepsilon_{eff} = \frac{\int A(\nu) \, d\nu}{\frac{1}{50} \int \frac{A(\nu)}{3780-\nu} d\nu}$$

Equation 9

For the unirradiated olivine, ε_{eff} = 12370 ±3700 L mol^{-1} cm^{-2} (decadal) where the error was determined using the ±30% confidence interval suggested by Paterson (1982). This value for the integral molar absorption coefficient and the olivine peak position of 3548 cm^{-1} are nearly identical to those reported

by Koch-Muller (2006), who, after correcting for unpolarized measurements, give ε_{int} = 12,500 ± 1666 L mol^{-1} cm^{-2}. For SiO$_2$, where the SiOH band is narrower, the integral decadal molar absorption coefficient was taken directly from Davis et al (1996), ε_{int} = 10,100 ± 200 L mol^{-1} cm^{-2}. The absorption coefficients reported in the literature were obtained for samples of natural OH content, not for ion implanted samples. Our results below show that they cannot be more than 10% lower in our case since the OH produced by implantation must be one or less per incident proton. The average OH peak position for the silica glass was 3673 cm^{-1}, identical to that of Davis et al. The absorbance in San Carlos olivine peaked near ~3570 cm^{-1}, similar to previous studies [Bell et al 2003 ; Koch-Muller, 2006], but exhibited a broad-band structure without sharp peaks as seen in silicate glass spectra [Stolper, 1982].

The difference in absorbance spectra of irradiated and unirradiated samples was taken to determine the change in OH absorbance band. Using the known fluence of implanted ions, the OH yield per proton, Y, or fraction of H ions which combine to form hydroxyl groups in the solid, was calculated by subtracting the calculated column density in the irradiated sample from that in the virgin sample and dividing by the total fluence F.

$$Y = \frac{\eta_{irradiated} - \eta_{virgin}}{F}$$

Equation 10

5.2 Results

Irradiation of the SiO$_2$ and mineral samples produced an increase in IR absorption depth of a 2.8 μm feature that correlates with the implantation fluence and plateaus after an implantation of >2x10^{17} H$^+$/cm^2. Figure 24 shows baseline corrected absorbance spectra for olivine and SiO$_2$ before and after irradiation with clear absorbance increases for both spectra.
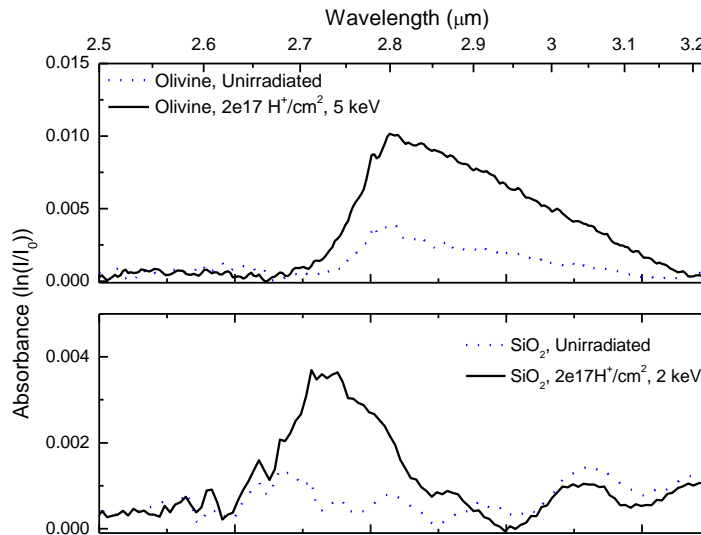
Figure 24. Spectra of unirradiated and irradiated olivine and amorphous silica. The SiO2 sample had no detectable OH band before irradiation while the olivine signal corresponded to an initial column density of 2x10^{16} OH/cm^2 (~4.3e^{17} OH/cm^3).

The SiO₂ samples used in the experiments had an initial OH concentration below detection limits and the resulting increase in absorption around 2.8 μm grew exponentially and can be attributed entirely to the H⁺ irradiation. The saturation column density is similar for SiO₂ implanted with 2 and 5 keV H⁺, though it is slightly greater for the higher energy implantation indicating an effect of ion energy on the number of bonds formed (Figure 25). The olivine sample has an initial OH absorption band depth of 0.0016 due to intrinsic water not removed during the vacuum bake. However, there is clearly an increase in band area after H⁺ irradiation that is larger than that for SiO₂ irradiated to the same fluence (Figure 24). The absorption bands produced by ion irradiation in olivine are broader than OH-bands found in many natural minerals, suggesting a broad distribution of bond strengths in the solid due to varying atomic configuration caused by radiation damage.
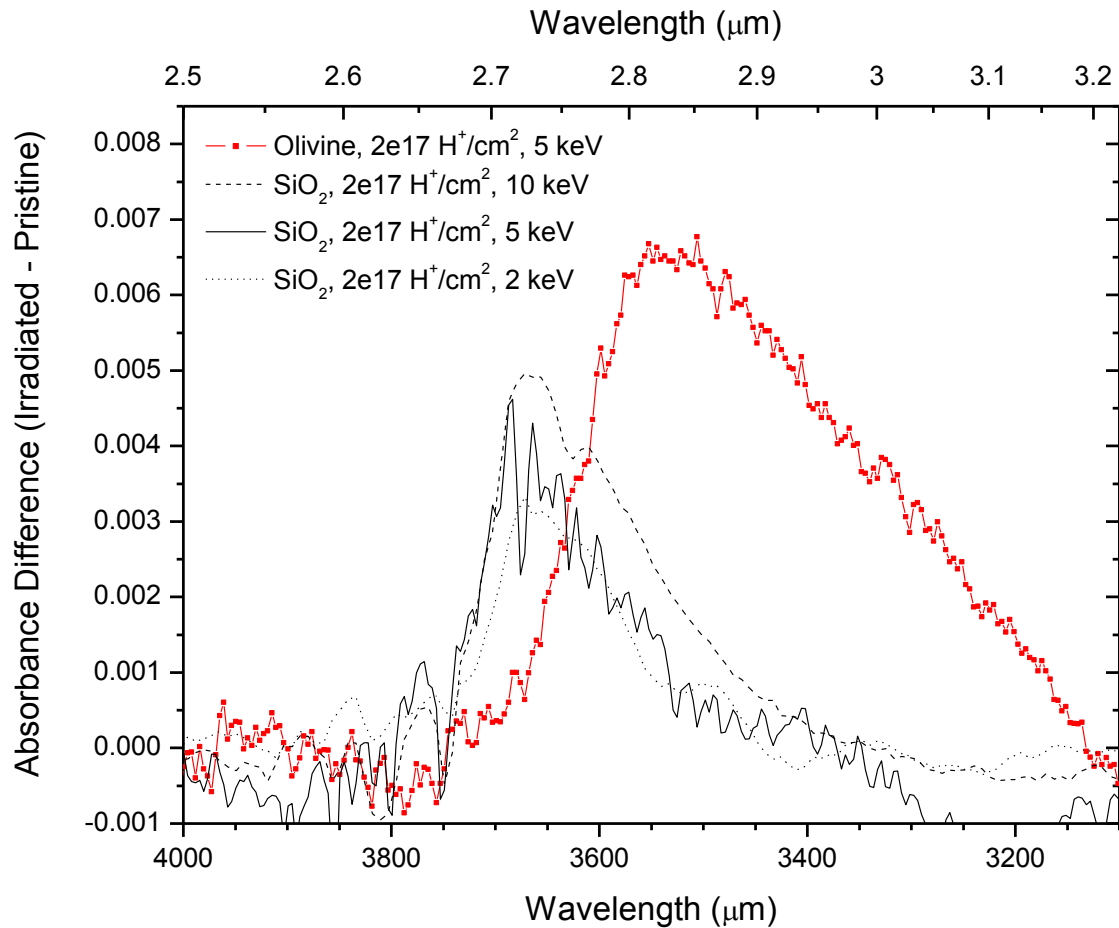

Figure 25. Difference in IR absorption calculated by subtracting the pristine from the irradiated spectra. Curves have been offset vertically for clarity. The labels denote peak positions.

5.2.1 Helium Irradiation and Sample Cooling

To provide additional verification that the increase in the OH absorption band was due to H⁺ implantation and not to radiation induced defects, SiO₂ was bombarded with 4 keV He⁺. At a fluence of 4×10^{17} He⁺/cm² there was no discernible change in the OH band region above the noise level (Figure 26A). The question of whether the implanted hydrogen can form H_2O molecules in addition to OH was

addressed by cooling the implanted samples to 15 K to determine if there was a change in the shape of the absorption band. This method has been used to determine the type of water (i.e. structurally bonded, point defects, or molecular water trapped in inclusions) in anhydrous minerals [Aines and Rossman, 1984]. By cooling the sample below 100K the water in inclusions freezes and the bands become much sharper, while there is only a minor effect on structural OH [Navarra et al., 2009]. Cooling of olivine samples to 15K after irradiation with fluences > 2 x 10^{17} H$^+$/cm^2 resulted in no significant change in the band shape, indicating that there were no large inclusions of water present (Figure 26). Furthermore, the slight shift toward lower wavenumbers could indicate the presence of hydrogen bonding at lower temperatures, although the shift could be within the noise. There was no evidence for an absorption near ~1900 cm^{-1} due to the H$_2$O bend absorption, again due to lack of sensitivity in the measurements, and the chemical state of the hydrogen, whether molecular water or OH, was not ultimately determined in this study.
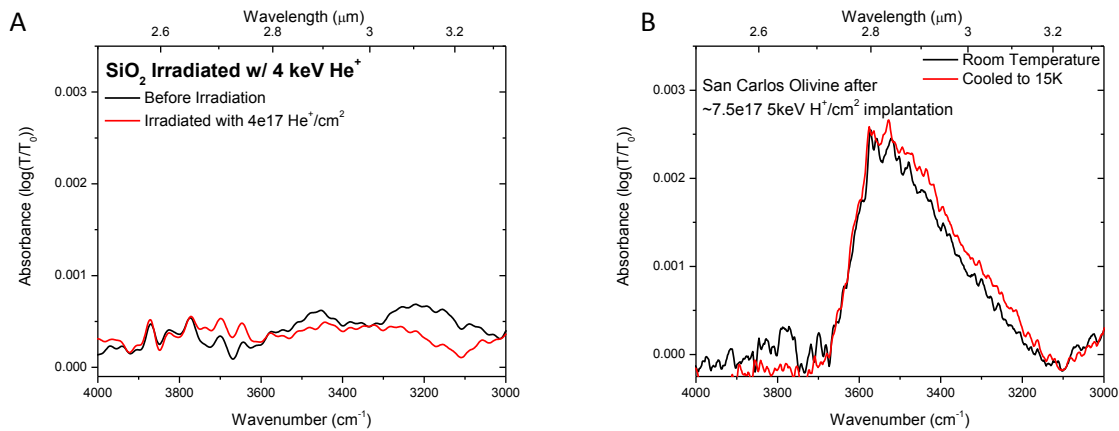
Figure 26. (A) Comparison of pristine vs. He irradiated SiO$_2$ spectra. The He irradiation causes no significant change in the region of the OH absorption. (B) Comparison of olivine spectra taken at room temperature (RT) and 15 K shows no significant change in the band shape indicating that H+ implantion produces only OH and not H$_2$O molecules.

Additionally, there was no evidence for the formation of a SiH stretching band, usually found in the 2300-2100cm^{-1} range, with an upper limit on the SiH absorbance depth of 0.0002 (0.005% transmittance), in agreement with Buemi et al. (1994). However, the SiO band at 1085cm^{-1} did change as a result of ion irradiation, decreasing the maximum band height while increasing the band width. The total band area remained constant within 1% and the peak maximum shifted ~8 cm^{-1} toward lower wavenumbers over the course of the irradiation. The band height decreases exponentially due to hydrogen implantation with a characteristic (1/e) fluence of 0.7(±0.1) 10^{16} ions/cm^2, which is the same, within error, to that for OH buildup. Irradiation with 5 keV Ar causes the band area to decrease linearly, as would be expected due to sputtering effects. Experiments done using 4keV He$^+$ again show an exponential decrease in peak height, though saturation doesn't occur until a greater fluence (4x10^{17} He$^+$/cm^2) than for proton implantation.

5.2.2 Sample Exposure to H₂ and Atmosphere

As mentioned above, one of the explanations offered for discrepancies in the measured hydroxyl production between the experiments of Burke et al (2011) and Ichimura et al (2012) was the exposure of irradiated samples to atmospheric air in the latter. To test the effects of background gas exposure during and after irradiation, samples were irradiated with He^+ and Ar^+ and subsequently exposed to background H_2 gas or atmospheric air. First, a sample was irradiated with 4×10^{17} He^+ (4 keV) and immediately removed to the pre-chamber which was then backfilled with high purity H_2 gas to a pressure of 1 Torr. The sample was left exposed to the H_2 for 12 hr, then returned to the main chamber and an IR spectra taken. The same sample was returned again to the pre-chamber which was then opened to atmosphere. The sample was left exposed to atmosphere for 1 hr, then re-analyzed under UHV to determine if there was an increase in absorption. Neither exposure produced a discernable difference in the 2.8 µm absorption region (Figure 27). To test the effect of background pressure during irradiation, a second sample was placed on the sample holder and the chamber backfilled with high purity H_2 to a pressure of 5×10^{-5} Torr. The sample was then irradiated with 5 keV Ar^+ to a fluence of 1×10^{17} Ar^+/cm^2 while maintaining constant the H_2 pressure in the chamber. After irradiation an IR spectra was taken and compared to the before spectra (Figure 28), and again no change in the irradiated spectra can be identified. However, it should be noted that the results may not be applicable to simulations using large ion currents which lead to OH formation from hydrogen incorporation, known to happen in minerals moderately heated (to 150 °C) in hydrogen (Cadenhear & Buerger, 1972).
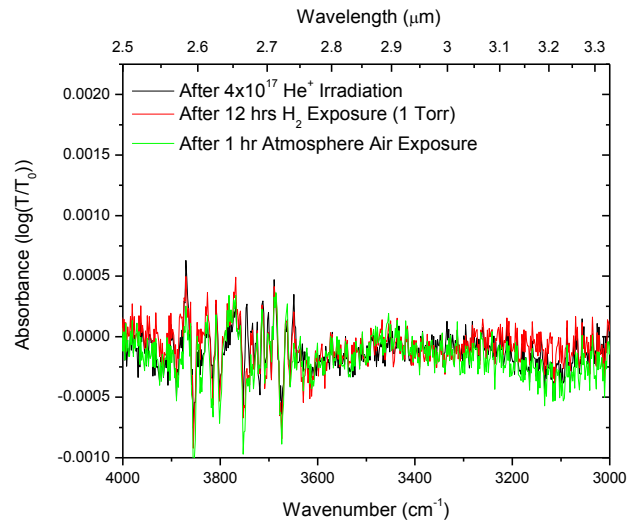

Figure 27: SiO₂ sample exposed to H₂ and atmospheric are after 4×10^{17} He⁺ irradiation. Exposure caused no discernable changes in the spectra.
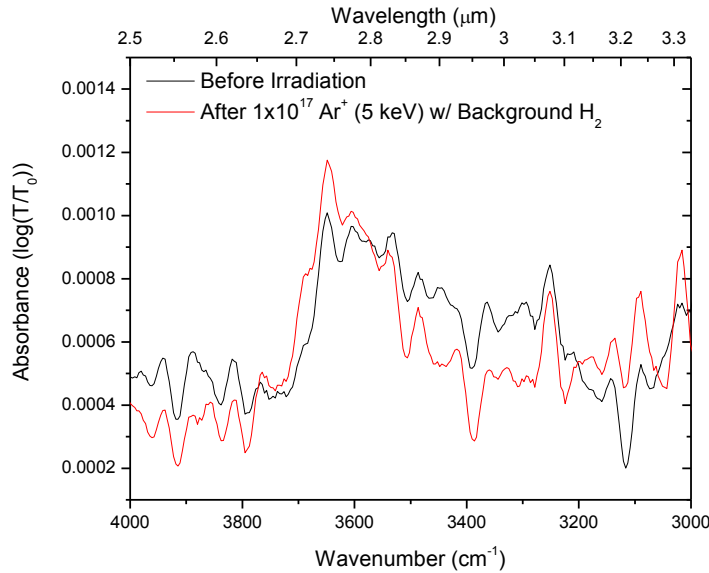
Figure 28: Before and after spectra of SiO$_2$ irradiated with 5 keV Ar$^+$ with an H$_2$ background pressure of 5x10^{-5} Torr during irradiation.

5.2.3   Water Band Growth

Hydrogen implantation produces an increase in both the OH-band peak height and integrated band area for absorptions centered at 3660 cm^{-1} (2.73 μm) in SiO$_2$ and ~3550 cm^{-1} (2.82 μm) in olivine. Both the band height and area increase exponentially up to a plateau at fluences of >2x10^{17} ions cm^{-2}. The average OH peak position for the amorphous silica was 3673 cm^{-1}, coincident with that of Davis et al. [1996]. The absorbance in San Carlos olivine peaks near ~3550 cm^{-1} similar to previous studies [Bell et al, 2003; Koch-Muller et al, 2006] but exhibits a broad-band structure without sharp peaks. The width of the OH band results from different configurations of the hydroxyl bonds in the solid giving different stretch frequencies [Plotnichenko et al, 2000] and its similarity to the electron beam deposited samples of Djouadi et al [2011] leads to the conclusion that the olivine structure is amorphous.The wider band for olivine than for SiO$_2$ is attributed at the wider variety of sites due to the additional cations (Mg, Fe) [Freund & Oberhauser, 1986]. Table 2 shows the column density increase, as well as the OH peak height, SiO peak height, and characteristic fluences for OH and SiO band changes.

As expected from a terrestrial mineral, the olivine sample had residual OH or water content due to intrinsic hydration not removed during the vacuum bake, that must be subtracted from the calculated amounts of OH formed by irradiation, and the OH band area increase after H$^+$ irradiation is larger than that for SiO$_2$ irradiated to the same fluence. The effect of the H$^+$ implantation can be determined by subtracting the un-irradiated spectra from the irradiated spectra (**Error! Reference source not found.**). The width of the OH absorption band produced by ion irradiation in olivine is larger than those found in many natural minerals, suggesting a broad distribution of bond strengths in the solid, possibly due to varying atomic configuration caused by radiation damage.

Many different methods were employed for fitting the OH peak areas. Primarily used was baseline subtraction using the OMNIC algorithm followed by band area integration and subtraction of the pristine OH band area to determine the band area increase due to H^+ implantation. Also used were FFT filtering (Origin Pro 8.0) to eliminate low frequency components in the spectra and, as shown in Figure 29, Gaussian curve fitting of the spectra.
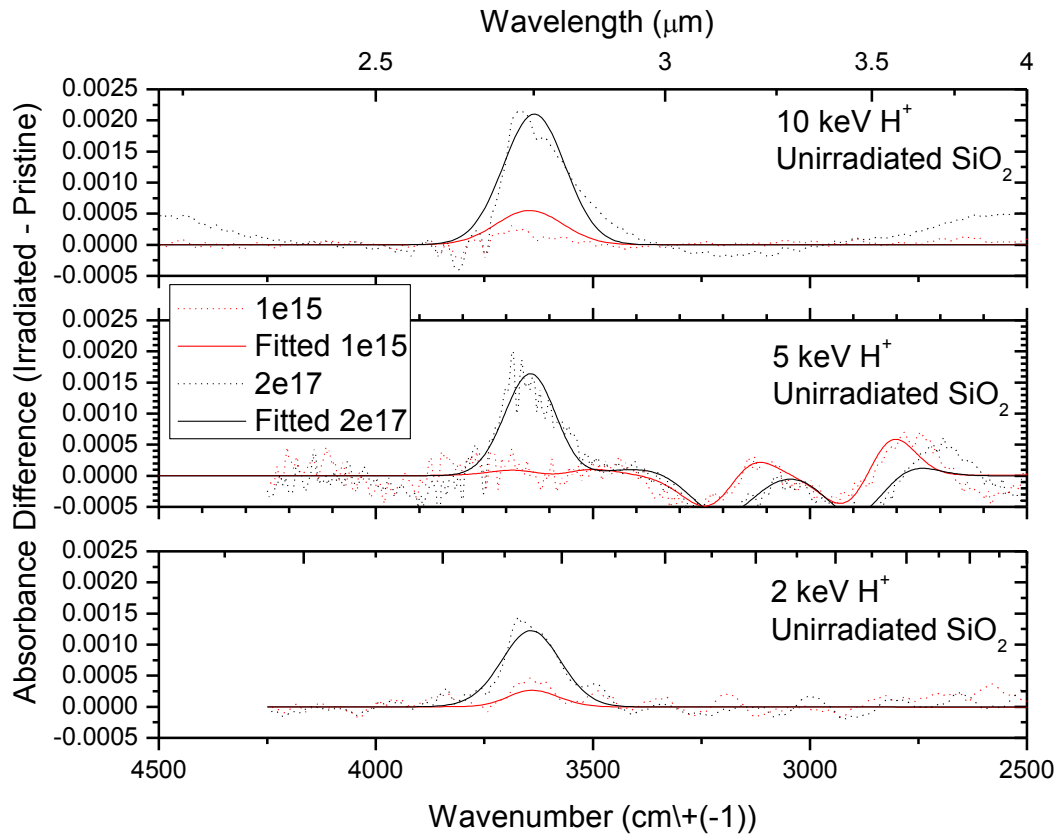

Figure 29. Gaussian curve fits of the main OH absorption spectra centered @ ~3650 cm⁻¹. Gaussian fits to 3 peaks were used for the 10 keV and 2 keV spectra (both collected at 16 cm⁻¹ resolution), while 6 peaks were used for the 5 keV spectra.

The implanted atoms can be incorporated into the mineral lattice at point defects, by bonding to lattice atoms, or as new molecules trapped in voids in the crystalline matrix. In the current work, implantation of 2-5 keV hydrogen into silica and mineral silicates analyzed in transmittance produced an increase in absorption band depth due to formation OH species. The Gaussian BA was determined for each of the spectra, and plotted vs. increasing fluence we see an exponential increase that seems to saturate after ~5×10^{16} H^+/cm^2 in SiO_2, and somewhat higher for olivine, though saturation fluences weren't reached for the mineral. Hydrogen implantation increases the OH-band absorbance peak height and integrated band area exponentially up to an apparent plateau at fluences of $>2 \times 10^{17}$ ions cm⁻² (Figure 30).
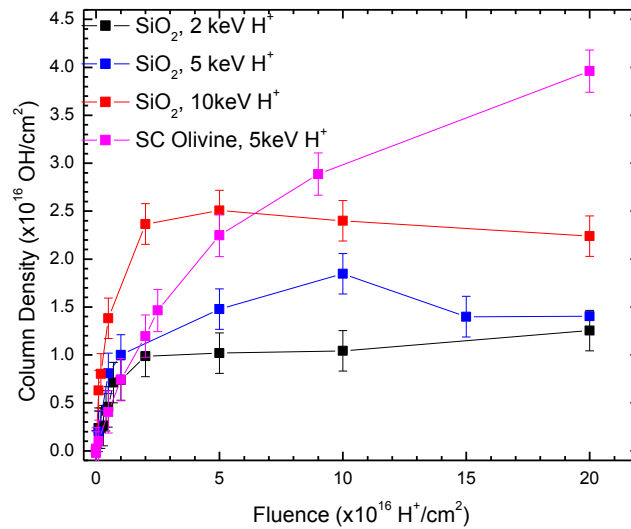
Figure 30. OH column density growth in SiO₂ and olivine irradiated with 2 and 5 keV H⁺. Note the saturation at large fluences.

The OH yield per implanted ion in both SiO_2 and olivine is initially as high as 0.9 OH bonds/proton and drops with fluence due to saturation. The column density in olivine after the same fluence of implanted hydrogen is approximately twice that of amorphous SiO_2 implanted with the same energy protons. The reason for the large uncertainty for the olivine column density is due to the integral molar absorption coefficient error of ±30% given by Paterson. The measured increase of η with fluence F is well fit by a the equation $\eta = \eta_s [1-\exp(-F/\tau)]$ where τ is the characteristic fluence. The olivine sample had the largest characteristic fluence, and was not fully saturated at fluences of 2×10^{17} H⁺/cm². For 2, 5 and 10 keV H⁺ implantation into pristine (unirradiated) amorphous SiO_2 the characteristic fluences were independent of the irradiation energy, within errors. The band increased exponentially up to a saturation that occurred after implantation fluences of ~1×10^{17} H⁺/cm², and the maximum band depth at saturation for H⁺ implantation into pristine (unirradiated) SiO_2 increases at higher energies corresponding to an increase in the saturation column density of OH (**Error! Reference source not found.**). The increased column density could be due to the larger implantation depth of the 5 and 10 keV H⁺ ions. Irradiation of sample with inert gas ions prior to H⁺ implantation also seemed to have an effect on the final OH column density, although the source of this effect was not entirely determined (Figure 31).
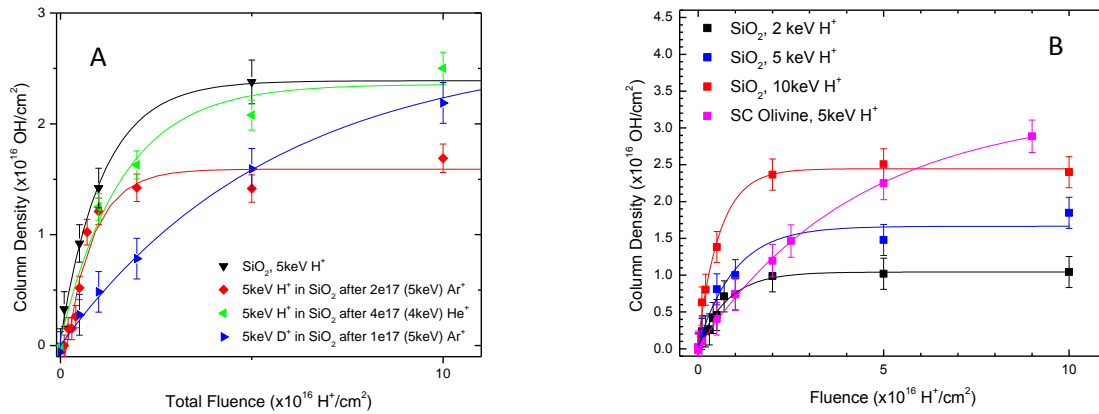
Figure 31: (A) Effect of irradiation with He+ and Ar+ prior to H+ implantation on OH column density. Irradiation with inert gas ions appears to reduce the maximum column density acheived as well as the approach to saturation. (B) The exponential increase saturates near 1×10^{17} H+/cm² and the saturation column density increases as the energy is increased. Olivine was not saturated even at fluences of 2×10^{17} H+/cm².

Table 2. . Column density increase, characteristic fluence and Si-O band peak height decrease for pristine and pre-irradiated SiO₂ and olivine samples implanted with H+

Implantation Fluence 1×10^{17} H+/cm²	H+ Implantation Energy [keV]	Column Density Increase [$\times 10^{16}$ OH/cm²]	OH Band Characteristic Fluence [$\times 10^{15}$ H+/cm²]	Maximum OH Band Depth [$\times 10^{-3}$ abs]	Si-O Peak Height Decrease [abs]	Si-O Peak Characteristic Fluence [$\times 10^{15}$ H+/cm²]
SiO₂ – Pristine	2	1.0 ±0.1	7.9 ±0.9	3.2 ±0.2	0.149 ±0.002	7.5 ±0.7
SiO₂ – Pristine	5	1.8 ±0.2	11.0 ±0.6	5.4 ±0.1	0.266 ±0.002	4.6 ±0.5
SiO₂ – Ar irradiated	5	1.7 ±0.1	9.7 ±2.8	3.9 ±0.2	0.222 ±0.002	9.2 ±0.8
SiO₂ – Pristine	10	2.4 ±0.3	5.8 ±0.8	5.1 ±0.2	0.378 ±0.002	2.3 ±0.2
San Carlos Olivine	5	3.2 ±1.4	52 ±5.1	6.7 ±0.1	- -	-
SiO₂ – Irradiated w/ >2e17H+, exposed to air, flipped and THEN irradiated with 5 keV D+	5	2.2 ±0.2	56 ±4.4	2.1 ±0.2	0.108 ±0.002	3.9 ±0.2

Irradiation of SiO₂ with D+ caused an increase in the band area peak at ~3200 cm⁻¹. The band area also increased exponentially, though it did not saturate the same as H+ implantation into SiO₂ and was more similar to the olivine instead. However, the column density after 1×10^{17} H+/cm² is similar to that for H+ implanted into pristine SiO₂ (Table 2). One possible source of error for the OH band could be fluctuations in the $H_2O_{(v)}$ concentration in the box. Even small variations in the amount of water vapor in

the ~36.5" IR beam path, not counting distance traveled under UHV, could influences the spectra in the 3600-4000 cm^{-1} region.
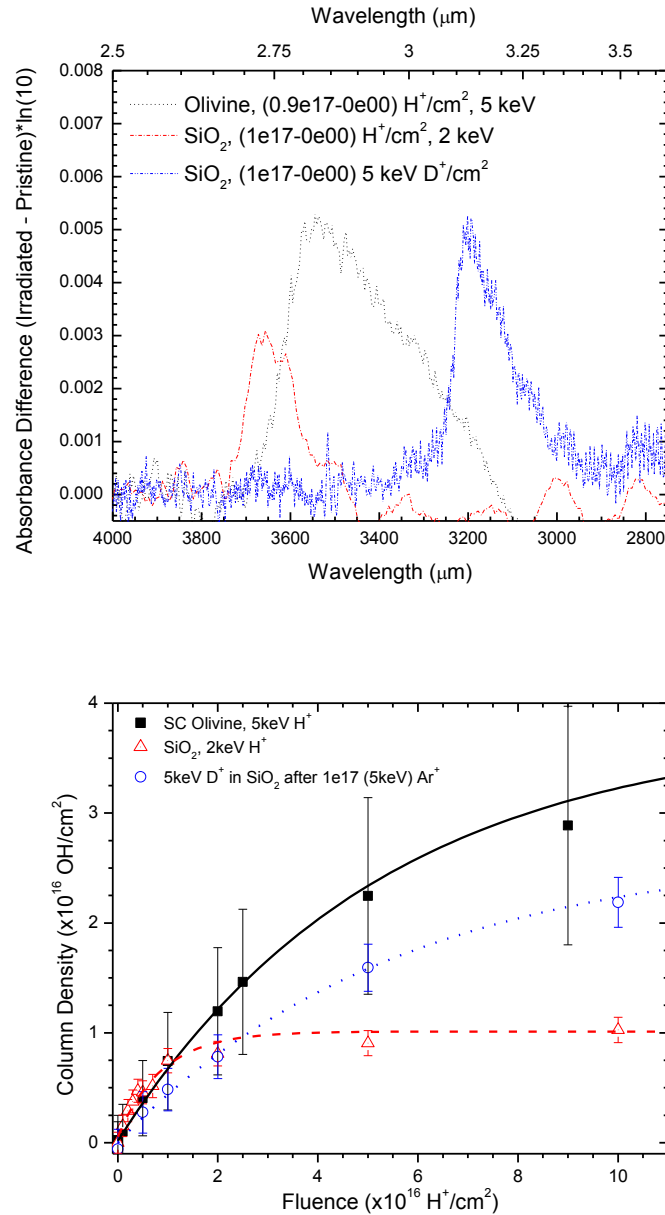
**Figure 32: Growth of the OH band in olivine and SiO₂ irradiated with H⁺ and D⁺ ions. The top image shows band area differences taken after H⁺ implantation fluences of 1x10¹⁷. The D⁺ peak center is at ~3200 cm⁻¹, while the H⁺ is peaked at ~3650 cm⁻¹, a shift of 56 meV. The bottom image shows that the OD band approach to saturation is more similar to the H⁺ peak in olivine.**

5.2.4 Changes in the Si-O absorption band

The SiO band at 1085 cm^{-1} decreased in height and increased in width upon ion irradiation while the total band area remained approximately constant, within ~1% pr the total band area. The position of the peak maximum appeared to shift ~8cm^{-1} toward lower wavenumbers over the course of the

irradiation. However, the high frequency edge was effectively constant, and on taking the spectral different (irradiated – pristine), the spectra indicate that the changes are due to the growth of a second peak at lower frequencies. This peak is absent in Ar$^+$ irradiated SiO$_2$, and thus it is attributed to the Si-OH stretch shifted to low frequencies by H-bonding in silanol (SiOH). The band height decreases exponentially due to hydrogen implantation with a characteristic fluence which is the same, within error, to that for OH buildup. For noble gas ions, irradiation produces a linear decrease in peak height but no band shift. This is explained by the thinning of the silicon oxide layer on Si as a result of sputtering.
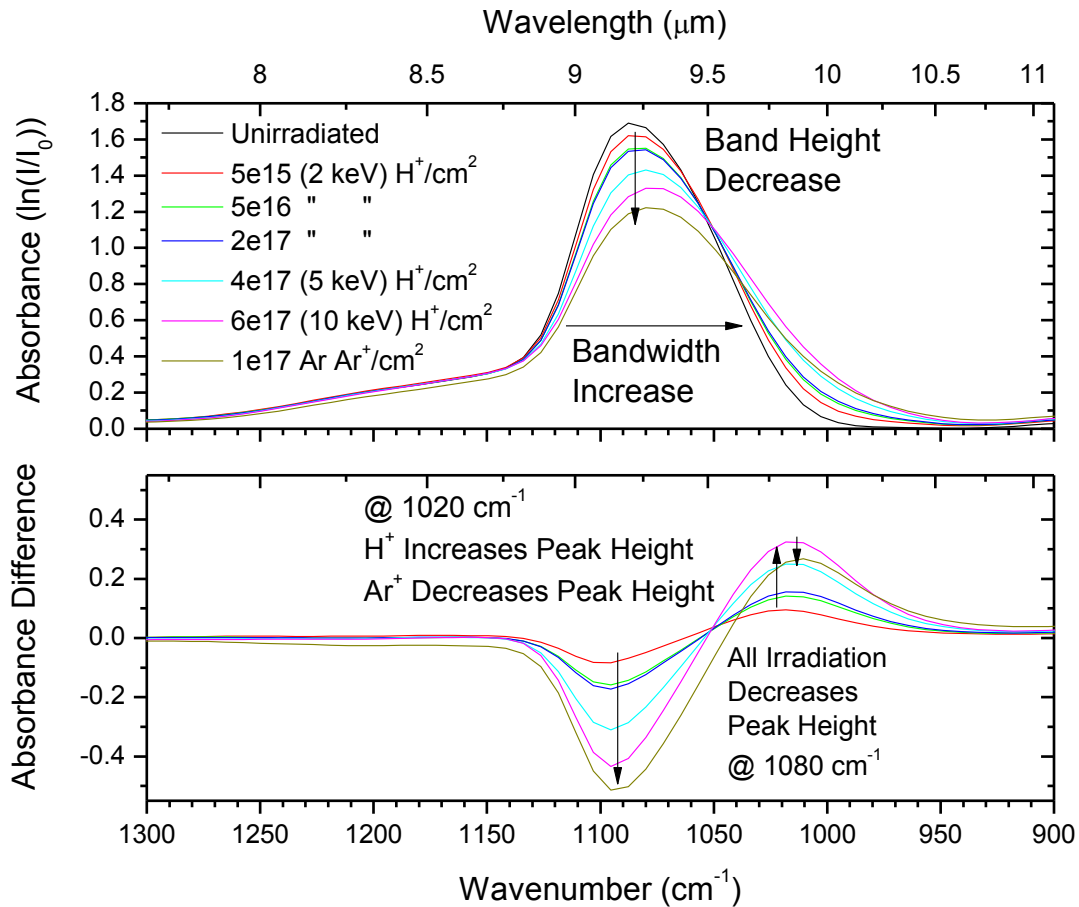
Figure 33. Changes in the SiO absorption band as a function of wavenumber and increasing irradiation fluence. H$^+$ implantation causes an exponential decrease in the main Si-O peak heat (~1080 cm^{-1}) with a corresponding increase in the absorbance at ~1020 cm^{-1}. Inert gas irradiation (Ar$^+$) causes a linear decrease in both SiO peaks (1080 cm^{-1} and 1020cm^{-1})

Changes in the Si-O band peak height follows similar trends as the OH band growth, with the peak height decreasing more at higher implantation energies (Figure 34). However, while the characteristic fluence for the OH band growth showed no definite trends, the saturation fluence for the SiO band peak height difference decreased with increasing energy, indicating that saturation was reached more quickly at higher energies (Table 2).
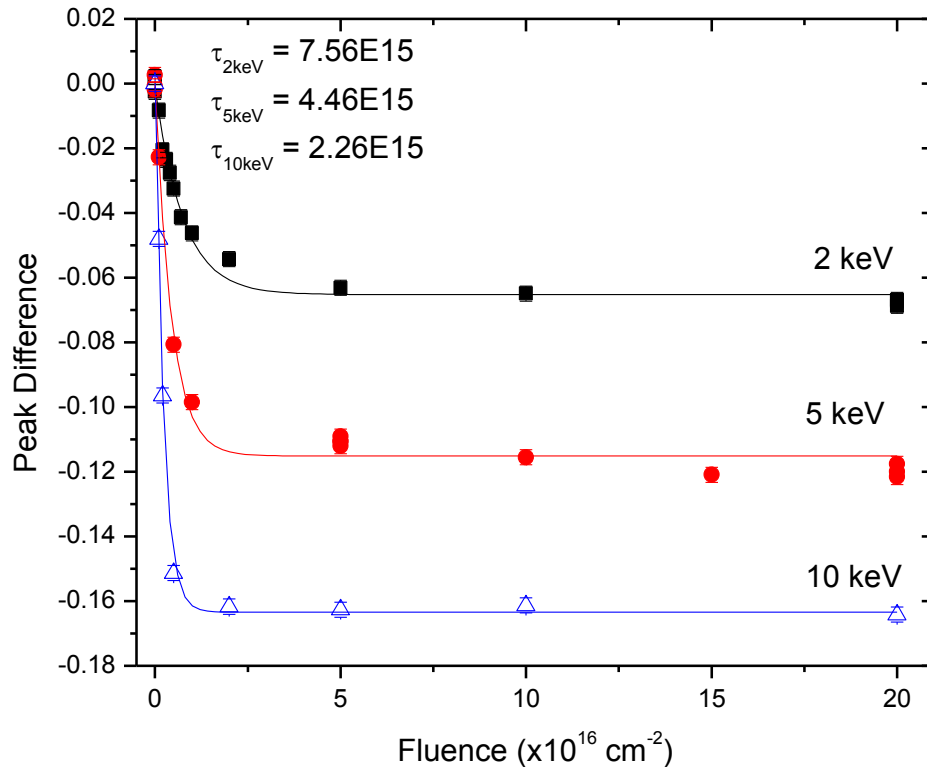
Figure 34. Decrease of SiO peak amplitude with increasing proton fluence in amorphous SiO$_2$ with 2, 5, and 10 keV H$^+$ ions.

5.2.5 Effects of irradiation with noble-gas ions

As can be seen in Figure 31A, amorphous SiO$_2$ pre-irradiated with 4 keV He$^+$ reached a similar saturation column density as the pristine samples and the characteristic fluence was the same within error. Pre-irradiation with 5 keV Ar caused a decrease in the saturation column density and the characteristic fluence was larger. In addition, H$^+$ implantation into unirradiated SiO$_2$ produced a greater change in the SiO band peak height than SiO$_2$ that had been irradiated with 5 keV Ar$^+$, the same as the trend described for the OH stretch band (Table 2). The effect of Ar$^+$ irradiation on the Si-O band was distinctly different than for the H$^+$ irradiation. The Ar$^+$ produced a decrease in the in the 1085 cm^{-1} band with no corresponding increase at 1018 cm^{-1} as seen in the H$^+$ implanted samples. Both the growth of the 1018 cm^{-1} and the decrease in the 1085 cm^{-1} band were exponential, while the decrease in the band peak height was linear for Ar$^+$. Irradiation of SiO$_2$ with 5 keV Ar$^+$ after H$^+$ implantation produced a linear decrease in both bands.
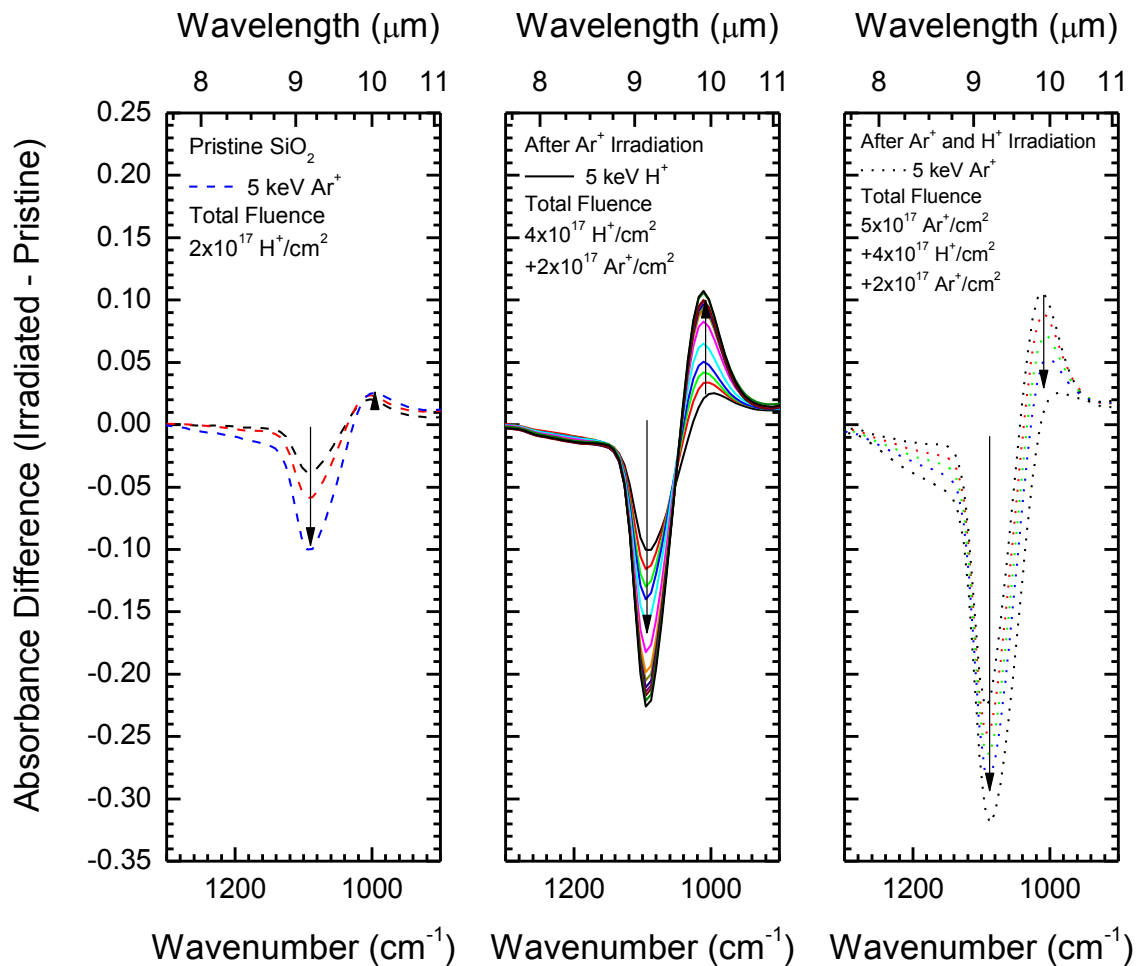
Figure 35. Changes in the SiO band as determined by spectral differences. Initial Ar irradiation drecreases both peaks, while 5 keV H+ implantation causes an exponential decrease in the 1080 cm-1 band area with a corresponding increase in the 1020 cm-1 band. The final Ar+ irradiation again decreases the spectra at all wavelengths in the SiO band region (~1300-900 cm-1).

Hydrogen implantation causes the peak height to decrease exponentially, and the behavior of the peak height change depends on the type of radiation ion and possibly the radiation history. It has already been noted that OH column density increase in amorphous SiO_2 was found to be decrease after prior inert Ar^+ processing, though He^+ irradiation showed only a change in the approach to saturation (Figure 31A). Irradiation with 5 keV Ar causes a distinctly linear decrease in the peak height, likely due to sputter removal of the amorphous layer. Additionally, the slope of the SiO peak area after H^+ implantation is somewhat decreased in comparison to 5 keV Ar^+ irradiation of pristine SiO_2. However, whether this difference was due to matrix effects of H^+ implantation or was simply an error in the measurements was not ultimately determined. Sequential irradiations of a single a-SiO_2 sample with 5 keV Ar^+ to a fluence of $2x10^{17}$, 5 keV H^+ to an addition $4x10^{17}$, and finally 5 keV Ar^+ an another $5x10^{17}$ for a total fluence of $11x10^{17}$ ions/cm^2 are shown in Figure 36.
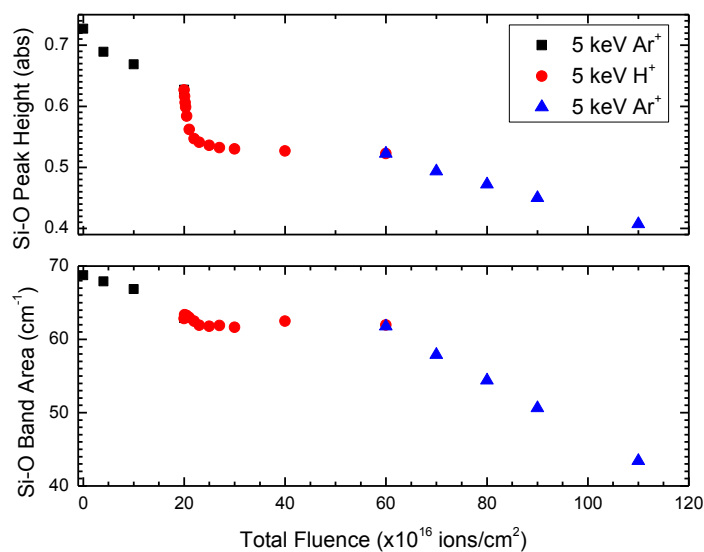
Figure 36. Changes in the SiO band as both a function of fluence and ion type. The Ar⁺ irradiation produces a linear decrease in both peak height and band area, while H⁺ gives an exponential decrease in the band height at ~1080 cm⁻¹ while the band area stay effectively constant.

6   Discussion

Previous work by Burke et al. (2011), also performed under ultrahigh vacuum, looked for OH production in terrestrial ilmenite and anorthite using reflectance infrared spectroscopy. They concluded that solar wind hydrogen implantation was unable to produce a sufficient 3μm absorption peak to account for the 2009 lunar observations. Rather, a decrease in the absorption signal was reported in some cases and attributed to the sputtering of adsorbed water. However, subsequent results by Djouadi et al. (2011) and Ichimura et al. (2012) showed that solar wind energy hydrogen (and deuterium) implantation in minerals and lunar soils causes a clear increase in the 3 μm absorption band. The sputtering cross section measured in Section 4 is irrelevant to the OH produced by H implantation as the radiation induced molecules are formed at depth in the material (100 to 1000 monolayers), while the sputtering of molecules occurs only for the top few monolayers. Furthermore, sputtering for an SiO_2 target by 1 keV Ar ions is ~1 atom/ion, meaning that at a fluence of $2x10^{17}$ ions/cm² a total of ~200 monolayers have been removed while only a few monolayers should be sputtered by the sample fluence of protons due to a much smaller sputtering yield [Johnson & Baragiola, 1991]. Thus, the sputter removal of OH molecules formed by H implantation is considered to be negligible.

The implanted atoms can be incorporated into the mineral lattice at point defects, by bonding to lattice atoms, or as new molecules trapped in voids in the crystalline matrix. In the current work, implantation of 2-5 keV hydrogen into silica and mineral silicates analyzed in transmittance produced an increase in absorption band depth due to formation OH species, and this increase was quantified as a function of fluence. The band increased exponentially up to a saturation that occurred after implantation fluences of ~$2x10^{17}$ H⁺/cm². The maximum band depth in transmittance at saturation is

0.4% for 2 keV implanted in pristine SiO_2 (corresponding to a column density increase of 1.2 ± 0.1 x10^{16} OH/cm^2) and 0.67% after 5 keV H$^+$ irradiation of olivine (4.0±0.2 x10^{16} OH/cm^2). These maximum depths are several times higher than the upper limit of 0.1% in reflection of Burke et al (2011) but a factor of 10 less than what was reported by Ichimura et al (2012). Djouadi et al (2011) reported a band depth increase in transmission of ~0.2% for olivine thin films irradiated to slightly higher fluences (3x10^{17}) with a distribution of ion energies in the range 1.5-5 keV. Their reported column density was a factor of 10 less due to the use of a single integral molar absorption coefficient (168,616 L mol^{-1} cm^{-2}), taken from a measurement of the absolute OH absorption strength in glycolic (carboxylic) acid. This highlights the importance of selecting the appropriate absorption coefficient for OH in minerals when reporting results. The calculated yield also depended on implantation energy and whether or not the sample had been irradiated prior to hydrogen implantation. At an implantation fluence of 1x10^{17} H$^+$/cm^2, the percent of implanted H that has been converted to OH is 10% for 2 keV H implanted in pristine SiO_2, 18% for 5 keV H$^+$ implanted in pristine SiO_2, and 17% for SiO_2 has been pre-irradiated with 2x10^{17} (5keV) Ar$^+$/cm^2.

The implantation column densities at saturation are less than the maximum value calculated in earlier (1x10^{17} OH/cm^2), but the explanation for this is partially due to the average implantation depth of the ions being less than the 100 nm used for the calculation, and also because the distribution of implanted ions is not uniform over the irradiation region but follows instead a nearly Gaussian profile. The absorbance band depth in olivine increases 0.003 (0.69% transmittance), higher than the limit set by Burke et al. (2011) but a factor of 10 less than what was found by Ichimura et al. (2012). The column density measured in olivine, 3.96(±0.14) x10^{16} OH/cm^2) after an implantation fluence of 2x10^{17} H$^+$/cm^2 corresponds to ~10% of the total implanted hydrogen being converted into hydroxide species. Djouadi et al (2011) reported a band depth increase of ~0.002 for olivine thin films irradiated to slightly higher fluences (3x10^{17}) with a distribution of ion energies in the range 1.5-5 keV. Their reported column density was a factor of 10 less due to the use of a single integral molar absorption coefficient (168,616 L mol^{-1} cm^{-2}), taken from a measurement of the absolute OH absorption strength in glycolic (carboxylic) acid. This highlights the need to take care when selecting the appropriate absorption coefficient for OH in minerals when reporting results.

Using the saturated column density in olivine, we can estimate the band area for a sample of uniformly irradiated lunar soil with an average particle size *r*. Assuming the implanted hydrogen formed a uniform layer of OH to a depth of *t* in the grains and that light penetrates the soil to a depth *d* > t, we can determine the equivalent column density to be

$$\eta_{OH,powder} = \frac{\eta_{OH,ol} \times d}{r}$$ **Equation 11**

Then, using an attenuation length of light in the soil of *d = 240 µm* [Shkuratov, 1999] and an average of 5 grains traversed (*r~48 µm*) [Burke et al, 2011], the expected column density will be 4 x10^{17} OH/cm^2. Relating the band depth of olivine to the column density increase due to hydrogen implantation and multiplying by 2 for reflection, we can determine the percent reflectance decrease for the powder to be

~2.4%, sufficient to explain many of the lunar surface measurements, but less than the measurements of Ichimura et al. (2012).

7   Conclusion

There are several sources of water on the Moon, and solar wind ions can affect the distribution of water across the lunar surface. Water deposited by meteorites or comets which impact the surface of the moon comes to rest on the surface of regolith grains where it is vulnerable to space weathering elements and may be photodesorbed by UV photons or sputter removed by solar wind ions. The desorbed water then moved in a random trajectory across the Moon until it either encounters a cold trap on the lunar poles, or is ejected from the surface with sufficient energy to escape the lunar gravity well. Water that is trapped in polar cold traps can also be effected by solar wind ions due to large electric fields that develop in the craters drawing ions in which then impact the surface and effect the molecules there [Zimmermann, 2011]. The measured cross-section of a water molecule on lunar soil at 80 K was $3x10^{-15}$ cm^2 for multiple (>1) adsorbed monolayers and $1x10^{16}$ cm^2 during the removal of the final monolayer.

Irradiation of silicate solids with 2-5 keV H^+ ions leads to the formation of SiOH complexes which can be identified using transmittance FTIR spectroscopy. There is no evidence for the formation of water. Both the depth and area of the OH absorption band grows with an exponentially decaying rate up to a fluence of $\sim 2x10^{17}$ H^+/cm^2, at which point the band saturates. Protons implanted into pristine samples form SiOH groups with near unit efficiency. As the number of oxygen available for new bonds decreases with irradiation fluence, the efficiency drops exponentially.

Pre-irradiation of samples with 4keV He^+ produces no change in the 2.8 µm absorption band, though it does cause a decrease in height and increase in bandwidth for the SiO band at ~9.25 µm. Proton implantation also decreases the SiO band height and has a more pronounced effect than the He irradiation.

Cooling implanted samples to cryogenic temperatures produces no significant change in the band shape, indicating the signal is due entirely to SiOH and not molecular water. Irradiation of samples with 4 keV He^+ produces no change in the 3 µm absorption signal, though it does cause a decrease in height and increase in bandwidth for the SiO band at ~9.25 µm. Proton implantation also decreases the SiO band height and has a more pronounced effect than the He irradiation. This is due to replacement of SiO bonds with OH bonds, while in the case of He irradiation the changes are due entirely to point defects and loss of bonds due to sputtering of oxygen from the sample surface. Though measurements were taken on solid sections of terrestrial minerals, we estimate the maximum absorption signal due to solar wind H^+ implantation in fully processed lunar soil with an average grain size of 45 µm to be 5%.

8   Future work

The primary need in the immediate future is the continuation of implantation experiments on SiO_2 and natural mineral samples in order to determine the effects of pre-irradiation, OH band

formation, SiO band shifts and isotope effects due to D$^+$ implantation. These experiments should be carried out on a in a careful manner so that accurate determinations of atmospheric exposure effects can be determined and minimized. Suggested terrestrial mineral analogs suggested for these transmission type experiments include, natural quartz, anorthite, ilmenile, albite and labradorite. Thin sections should be ground to a minimum transparent thickness while still maintaining rigidity, and baking the samples at high temperatures (>900K) under high vacuum could be used to minimize interstitial water and surface contamination. Studies could also be carried out using a hydrogen plasma to bombard the surface, or pre/post irradiation with a lyman-alpha UV lamp or a higher energy UV laser. The FTIR results should be complimented by SIMS measurements to determine the depth profile of formed OH species for the implanted samples.

Another method used to student OH formation in silicates is computational modeling. One type of computational model that can be used to study these interactions is molecular dynamics (MD). In MD simulations, Newton's equations of motion are used to trace the path of each impacting ion as it enters the solid by calculating the interactions of the impacting atoms with the solid atoms in the immediate neighborhood of the impact site and subsequent damage track, and the resulting motions of excited atoms throughout the solid. As such, MD is a computationally intensive technique and only a few ion impacts onto small blocks of matter can be simulated at a time. This can be improved using parallel computing techniques.

Work on this has begun in the form of a Molecular Dynamics program capable of simulating ion bombardment of silicate solids and silicate water mixtures. The program uses a variety of standard atomic interaction potentials such as the Stillinger-Webber potential for silicon atoms [Stillinger and Webber, 1985], the Zeigler-Beirshak-Littmark potential for ion-solid interactions [Zeigler *et al.*, 1985], as well as a potential developed by S. H. Garofalini which can simulate the interactions of SiO2 + H2O mixtures [Feuston and Garofalini, 1988]. The goal of the simulational work will be to model ion implantation in amorphous SiO$_2$, similar to the experiments presented above, in order to determine the fate of the implanted ions and how ion implantation changes the nature of the solid, either through long-lived electronic excitations, nuclear displacements, or electron emission and molecular desorption.

9 References

Aines, R.D, G.R. Rossman (1984), "Water in minerals? A peak in the infrared." Journal of Geophysical Research, 89, B6

Allodi, M.A. et al. (2013), "Complementary and Emerging Techniques for Astrophysical Ices Processed in the Laboratory." Space Science Reviews, 180: 101-175

Andersson, S. and E.F. van Dishoeck (2008), "Photodesorption of water ice." Astronomy and Astrophysics, 491: 907-916

Arnold, J. R. (1979). "Ice in the Lunar Polar Regions." Journal of Geophysical Research 84, NB10: 5659-5668.

Baragiola, R.A., M.J. Loeffler, U. Raut, et al. (2005), "Laboratory studies of radiation effects in water ice in the outer solar system." Radiation Physics and Chemistry, 72, 187

Bell, D.R., et al. (2003), "Hydroxide in olivine: A quantitative determination of the absolute amount and calibration of the IR spectrum." Journal of Geophysical Research, 108

Bennett, C.J., et al. (2006), "Laboratory studies on the irradiation of methane in interstellar, cometary, and solar system ices." Astrophysical Journal, 653, 1

Bennett, C.J., C. Pirim, T.M. Orlando (2013), "Space-Weathering of Solar System Bodies: A Laboratory Perspective." Chemical Reviews, 113: 9086

Besse, S., et al. (2013), A visible and near-infrared photometric correction for Moon Mineralogy Mapper (M^3)." Icarus, 222, 1

Bibring, J.P., et al. (1982), "Synthesis of molecules by irradiation in silicates." Journal of Geophysical Research, 87

Boyce, J.W., et al (2010), "Lunar apetite with terrestrial volatile abundances." Nature, 466: 466-469

Buemi, A., Cimino, G., Leto, G., and Strazzullaa, G. 1994, "On the observability of –SiH vibrational stretch on solid objects in the Solar System." Icarus 108: 169

Burke, D.J., et al. (2011), "Solar wind contribution to surficial lunar water: Laboratory investigations." Icarus, 211

Cadenhead, D.A. and W.G. Buergel (1973), "Water Vapor from a Lullar Breccia: Implications for Evolving Planetary Atmospheres." Science 180: 1166.

Cantando, E.D., et al. (2008), "Aqueous depletion of Mg from olivine surfaces enhanced by ion irradiation." Journal of Geophysical Research, 113

Cassidy, T.A., Johnson, R.E., 2005. Monte Carlo model of sputtering and other ejection processes with a regolith. Icarus, 176: 499–507

Clark, R.N. (2009), "Detection of Adsorbed Water and Hydroxyl on the Moon." Science, 326: 5952

Clark, R.N., et al. (2011), "Thermal removal from near-infrared imaging spectroscopy data of the Moon." Journal of Geophysical Research-Planets, 116, E00G16

Colaprete, A., et al. (2010), "Detection of water in the LCROSS ejecta plume." Science, 330: 6003

Crider, D.H. and R.R. Vondrak (2000), "The solar wind as a possible source of lunar polar hydrogen deposits." Journal of Geophysical Research, 105, E11

Davis, K.M., et al. (1996), "Quantitative infrared spectroscopic measurement of hydroxyl concentrations in silica glass." Journal of Non-Crystalline Solids, 203

Davoisne, C., et al. (2008), "Chemical and morphological evolution of a silicate surface under low-energy ion irradiation." Astronomy and Astrophysics, 482: 541-548

Demyk, K., et al. (2004), "IR spectroscopic study of olivine, enstatite, and diopside irradiated with low energy H^+ and He^+ ions." Astronomy and Astrophysics, 420: 233

Dienes, G.J. and A.C. Damask (1958), "Radiation Enhanced Diffusion in Solids." Journal of Applied Physics, 29: 1713

Djouadi, Z., et al. (2011), "Hydroxyl radical production and storage in analogues of amorphous interstellar silicates." Astronomy and Astrophysics, 531

Dukes, C.A., R.A. Baragiola, L.A. McFadden (1999), "Surface modification of olivine by H^+ and He^+ bombardment." Journal of Geophysical Research, 104, E1

Dukes, C.A. et al. (2011), "Laboratory studies on the sputtering contribution to the sodium atmospheres of Mercury and the Moon." Icarus, 212: 463-469

Epstein, S., H.P. Taylor Jr. (1975), "Carbon, hydrogen, oxygen and silicon isotope relationships in the lunar regolith." Lunar and Planetary Science Conference Proceedings, 6: 254

Famá, M., J. Shi, R.A. Baragiola, 2008. Sputtering of ice by low-energy ions. Surface Science 602: 156–161

Feldman, W. C., D. J. Lawrence, et al, (2000). "Polar hydrogen deposits on the Moon." Journal of Geophysical Research-Planets 105, E2: 4175-4195.

Fink, D., et al. (1995), "Hydrogen implantation and diffusion in silicon and silicon dioxide." Applied Physics A, 61: 381

Feuston, B. P., S. H. Garofalini (1988) "Empirical three-body potential for vitreous silica." Journal of Chemical Physics 89 (9): 5818-5824

Freund, F., Oberhauser, G. (1986) Water dissolved in olivine: a single-crystal infrared study, J. Geophys. Res. 91, 745

Futagami, T., Ozima, M., Nagai, S., Aoki, Y. (1993), Experiments on thermal release of implanted noble gases from minerals and their implications for noble gases in lunar soil grains, Geochimica et Cosmica Acta 57: 3177

Greenburg, J.M, A. Li, ed. *Proceedings of the NATO Advanced Study Institute on Formation and Evolution of Solids in Space*. March 1997. Erice, Silily, Italy. Kluwer Academic Publishers, 1999. 1st ed.

Grosjean, D.E., 1996. Luminescense, electron emission, and sputtering from ion-bombarded solid argon films. Ph.D. Thesis, University of Virginia, Charlottesville, VA

Gruen, D.M., B. Siskind, and R.B. Wright (1976), "Chemical implantation, isotopic trapping effects, and induced hygroscopicity resulting from 15 keV ion bombardment of sapphire." The Journal of Chemical Physics, 65, 1

Gupta, A. and G.N. Parsons (2000), "Bond strain, chemical induction, and OH incorporation in low-temperature (350-100°C) plasma deposited silicon dioxide films." Journal of Vacuum Science Technology B, 18, 3

Hapke, B. (2001). "Space weathering from Mercury to the asteroid belt." Journal of Geophysical Research-Planets 106, E5: 10039-10073.

Heiken, G.H., D.T. Vaniman, B.M. French (1991), "Lunar sourcebook – A user's guide to the moon." Cambridge University Press

Housley, R.M. and R.W. Grant (1976), "ESCA studies of the surface chemistry of lunar fines." Proceedings of the 7th Lunar Science Conference: 881-889

Housley, R.M. (1992), "XPS studies of the surface chemistry of lunar highlands regolith." Abstracts of the Lunar and Planetary Science Conference, 23: 557

Ichimura, A.S., et al. (2012), "Hydroxyl (OH) production on airless planetary bodies: Evidence from H^+/D^+ ion-beam experiments." Earth and Planetary Science Letters, 90: 345-348

Ioppolo, S., et al. (2008), "Laboratory evidence for efficient water formation in interstellar ices." The Astrophysical Journal, 686: 1474-1479

Johnson, R.E. (1990), "Energetic charged particle interactions with atmospheres and surfaces." Physics and Chemistry in Space v19 Planetology, Springer-Verlag Berlin Heidelburg

Johnson, R.E., and Baragiola, R.A. (1991), "Lunar surface: Sputtering and Secondary Ion Mass Spectrometry", Geophysical Research Letters 18: 2169.

Keller, L.P, and D.S. McKay (1997), "The nature and origin of rims on lunar soil grains." Geochemica et Comochimica Acta, 61, 11

Koch-Muller, M. et al. (2006), "Hydroxyl in mantle olivine xenocrysts from the Udachnaya kimberlite pipe." Physics and Chemistry of Minerals, 33: 276-287

Lanford, W.A. and C. Burman (1983), "Effects of ion implantation on the reaction between water and glass." Nuclear Instruments and Methods, 209/210

Laul, J.C. and R.A. Schmitt (1976), "Chemical composition of Apollo 15, 16, and 17 samples" Proceedings of the 4th Lunar Science Conference: 1349-1367

Leroux, H., 2009. Dust modification under photon, electron and ion irradiation. In *Interstellar dust from Astronomical Observations to Fundamental Studies*; Boulanger, F., Joblin, C., Jones, A., Madden, S., Eds.; EAS Publications Series; European Astronomical Society: Cambridge, U.K., 2009; Vol 35: 153-169

Libowitzky E. and G.R. Rossman (1996), "Priciples of quantitative absorbance measurements in anisotropic crystals." Physics and Chemistry of Minerals, 23, 6: 319-327

Liu, Y., et al. (2012), "Direct measurement of hydroxyl in the lunar regolith and the origin of lunar surface water." Nature Geoscience, 5, 11

Loeffler, M.J., et al. (2006), "Synthesis of hydrogen peroxide in water ice by ion irradiation." Icarus, 180: 265-273

Loeffler, M.J., C.A. Dukes, R.A. Baragiola, 2009. Irradiation of olivine by 4 keV He^+: Simulation of space weathering by the solar wind. Journal of Geophysical Research 114, E03003

Managadze, G.G., V.T. Cherepin, et al. (2011), "Simulating OH/H_2O formation by solar wind at the lunar surface." Icarus, 215: 499

Mattern, P.L., G.J. Thomas, W. Bauer (1975), "Hydrogen and helium implantation in vitreous silica." Journal of Vacuum Science Technology, 13, 1

Martinez, O., et al. (2009), "Experimental determination of the rate constant for the associative detachment reaction $H^- + H \rightarrow H_2 + e^-$ at 300 K." The Astrophysical Journal, 705: L172-L175

McCord, T.B., et al. (2011), "Sources and physical processes responsible for OH/H_2O in the lunar soil as revealed by the Moon Mineralogy Mapper (M^3)." Journal of Geophysical Research, 116

Mitchell, E.H., et al. (2013), "Ultraviolet photodesorption as a driver of water migration on the lunar surface." Planetary and Space Science, 89, 42

Moore, M.H., T. Tanabé, J.A. Nuth (1991), "The SiH vibrational stretch as an indicator of the chemical state of interstellar grains." Astrophysical Journal, 373

Morimoto, Y., et al. (1992), "Analysis of gas release from vitreous silica." Journal of Non-Crystalline Solids, 139, 35

Navarra, G., et al. (2009), "Temperature effects on the IR absorption bands of hydroxyl and deuteroxyl groups in silica glass." Journal of Non-Crystalline Solids, 355: 1028-1033

Oberg, K.I., et al. (2009a), "Formation rates of complex organics in UV irradiated CH_3OH-rich ices." Astronomy and Astrophysics, 504: 891-913

Oberg, K.I., et al (2009b), "Photodesorption of ices. II. H_2O and D_2O." The Astrophysical Journal, 693: 1209-1218

Ong, L., et al (2010), "Volatile retention from cometary impacts on the Moon." Icarus, 207, 2:578-589

Paterson, M.S. (1982), "The determination of hydroxyl by infrared absorption in quartz, silicate glasses and similar materials." Bulletin de Mineralogie, 105, 20

Pieters, C. M., E. M. Fischer, et al. (1993). "Optical Effects of Space Weathering - the Role of the Finest Fraction." Journal of Geophysical Research-Planets, 98, E11: 20817-20824.

Pieters, C.M., et al. (2009), "Character and Spatial Distribution of OH/H_2O on the Surface of the Moon Seen by M^3 on Chandrayaan-1." Science, 326: 5952

Plotnichenko, V.G., Sokolov, V.O., Dianov, E.M. (2000), Hydroxyl groups in high-purity silica glass, J. Non-Cryst. Solids 261, 186

Saal, A.E., et al. (2008), "Volatile content of lunar volcanic glasses and the presence of water in the Moon's interior." Nature, 454

Shang, L. et al. (2009), "Determination of diffusion coefficients of hydrogen in fused silica between 296 and 523 K by Raman spectroscopy and application of fused silica capillaries in studying redox reactions." Geochimica et Cosmochimica Acta, 73: 5435

Shi, J., et al. (2012), "Ion-induced electrostatic charging of ice at 15-160 K." Physical Review B, 83, 3

Shi, M., R.A. Baragiola, et al. (1995), "Sputtering of water ice surfaces and the production of extended neutral atmospheres." Journal of Geophysical Research-Planets, 100, E12: 26387-26395

Starukhina, L.V. (2001), "Water detection on atmosphereless celestial bodies: Alternative explanations of the observations." Journal of Geophysical Research, 106, E7

Stillinger, F. H., T. A. Webber (1985). "Computer simulation of local order in condensed phases of silicon." Physical Review B 31 (8): 5261-5271

Stolper, E. (1982), "Water in silicate glasses: An infrared spectroscopic study." Contributions to Mineralogy and Petrology, 81 :1-17

Strazzulla, G., J. R. Brucato, et al. (1995), "Interaction of Solar-Wind Ions with Planetary Surfaces. Laboratory Planetology." D. Mohlmann. 15: 13-17

Strycker, P.D., et al. (2013), "Characterization of the LCROSS implact plume from ground-based imaging detection." Nature Communications, 4, 2620

Sunshine, J.M., et al. (2009), "Temporal and Spatial Variability of Lunar Hydration as Observed by the Deep Impact Spacecraft." Science, 326: 5952

Taylor, L.A., G.R. Rossman, Q. Qi (1995), "Where has all the lunar water gone?" Lunar and Planetary Science Conference, 26: 1399

Theocharous, E. (2005), "Stability of spectral responsivity of cryogenically cooled InSb infrared detectors." Applied Optics 44: 6087

Watson, K., B.C. Murray, H. Brown (1961), "The behavior of volatiles on the lunar surface." Journal of Geophysical Research, 66, 9

Zeller, E.J., L.B. Ronca and P.W. Levy (1966). "Proton-induced hydroxyl formation on the lunar surface." Journal of Geophysical Research 71: 4855–4860

Ziegler, J. F. , J. P. Biersack, and U. Littmark, The Stopping and Range of Ions in Matter, volume 1, (Pergamon, New York, 1985)

Zimmerman, M.I., et al (2011), "Solar wind access to lunar polar craters: Feedback between surface charging and plasma expansion." Geophysical Research Letters, 38, L19202